

UNCLASSIFIED

AD NUMBER

AD820218

LIMITATION CHANGES

TO:

Approved for public release; distribution is unlimited.

FROM:

Distribution authorized to U.S. Gov't. agencies and their contractors;
Administrative/Operational Use; SEP 1967. Other requests shall be referred to Space and Missile Systems Organization, Los Angeles, CA.

AUTHORITY

SAMSO ltr 16 Aug 1973

THIS PAGE IS UNCLASSIFIED

AEDC-TR-67-178

OCT 4 1967

SEP 26 1968

OCT 1968

cy 4



BUFFET RESPONSE AND AERODYNAMIC DAMPING CHARACTERISTICS OF AEROELASTICALLY SCALED TITAN III/MOL CONFIGURATIONS AT TRANSONIC SPEEDS

J. E. Robertson and T. R. Brice
ARO, Inc.

September 1967

This document is subject to special export controls and each transmittal to foreign governments or foreign nationals may be made only with prior approval of SAMSO (SMSDM-1) STINFO, AF Unit P O, Los Angeles, California.

**PROPULSION WIND TUNNEL FACILITY
ARNOLD ENGINEERING DEVELOPMENT CENTER
AIR FORCE SYSTEMS COMMAND
ARNOLD AIR FORCE STATION, TENNESSEE**

PROPERTY OF U. S. AIR FORCE
AEDC LIBRARY
AF 40(600)1200

NOTICES

When U. S. Government drawings specifications, or other data are used for any purpose other than a definitely related Government procurement operation, the Government thereby incurs no responsibility nor any obligation whatsoever, and the fact that the Government may have formulated, furnished, or in any way supplied the said drawings, specifications, or other data, is not to be regarded by implication or otherwise, or in any manner licensing the holder or any other person or corporation, or conveying any rights or permission to manufacture, use, or sell any patented invention that may in any way be related thereto.

Qualified users may obtain copies of this report from the Defense Documentation Center.

References to named commercial products in this report are not to be considered in any sense as an endorsement of the product by the United States Air Force or the Government.

BUFFET RESPONSE AND AERODYNAMIC DAMPING
CHARACTERISTICS OF AEROELASTICALLY SCALED
TITAN III/MOL CONFIGURATIONS AT TRANSONIC SPEEDS

J. E. Robertson and T. R. Brice
ARO, Inc.

This document is subject to special export controls and each transmittal to foreign governments or foreign nationals may be made only with prior approval of SAMSO (SMSDM-1) STINFO, AF Unit PO, Los Angeles, California.

FOREWORD

The work reported herein was done at the request of SAMSO, Air Force Systems Command (AFSC), for the Aerospace Division of the Martin-Marietta Corporation, under Program Element 6440909F/624A.

The test results presented were obtained by ARO, Inc. (a subsidiary of Sverdrup & Parcel and Associates, Inc.), contract operator of the Arnold Engineering Development Center (AEDC), AFSC, Arnold Air Force Station, Tennessee, under Contract AF40(600)-1200. The test was conducted under ARO Project No. PB0605 from April 27 through May 19, 1967, and the manuscript was submitted for publication on August 9, 1967.

Information in this report is embargoed under the Department of State International Traffic in Arms Regulations. This report may be released to foreign governments by departments or agencies of the U. S. Government subject to approval of the SAMSO (SMSDM-1) STINFO, Los Angeles, California, or higher authority within the Department of the Air Force. Private individuals or firms require a Department of State export license.

This technical report has been reviewed and is approved.

Richard W. Bradley
Lt Col, USAF
AF Representative, PWT
Directorate of Test

Leonard T. Glaser
Colonel, USAF
Director of Test

ABSTRACT

A wind tunnel investigation was conducted to obtain the buffet response and aerodynamic damping of 0.07-scaled aeroelastic models of Titan III/MOL configurations at transonic Mach numbers. Buffet response results were obtained in the form of bending moments at a selected model station. Aerodynamic damping results were obtained by the forced-oscillation technique, whereby the elastic modes of the model were excited by an electromagnetic shaker, and the exciting force and resulting model acceleration were recorded. A phase separation technique was used to resolve the structural damping (air-off conditions) and combined structural and aerodynamic damping (air-on conditions) from the measured force and acceleration. The test was conducted in the Mach number range from 0.80 to 1.10 and at zero angle of attack. All configurations experienced peak buffet response near Mach number 0.95. The buffet response for the Gemini and SV-5 configurations agreed reasonably well with previous test results for the same or similar configurations. The aerodynamic damping was generally positive and varied with Mach number. The largest variations occurred in the Mach number range from 0.925 to 1.00 for the Gemini and SV-5 configurations. Increasing dynamic pressure caused an increase in aerodynamic damping, although the increase in damping was not necessarily proportional to dynamic pressure.

<p>This document is subject to special export controls and each transmittal to foreign governments or foreign nationals may be made only with prior approval of SAMSO (SMSDM-1) STINFO, AF Unit P O, Los Angeles, California.</p>

CONTENTS

	<u>Page</u>
ABSTRACT.	iii
NOMENCLATURE.	ix
I. INTRODUCTION	1
II. APPARATUS	
2.1 Test Facility.	1
2.2 Test Articles.	1
2.3 Instrumentation.	4
III. TEST DESCRIPTION	
3.1 Test Conditions.	7
3.2 Test Procedure.	7
3.3 Data Reduction	9
IV. RESULTS AND DISCUSSION	
4.1 Air-Off Vibration Testing	11
4.2 Buffet Response	13
4.3 Air-On Vibration Testing	13
V. CONCLUSIONS	15
REFERENCES	16

TABLE

I. Summary of Model Physical Properties	3
---	---

APPENDIXES

I. ILLUSTRATIONS

Figure

1. Schematic of the Model Installation in Tunnel 16T . . .	19
2. Photographs of the Various Configurations Installed in Tunnel 16T	
a. Configuration 42	19
b. Configuration 43	20
c. Configuration 44	20
d. Configuration 45	21
e. Configuration 46	21

<u>Figure</u>	<u>Page</u>
3. Details of the Titan III Booster.	22
4. Orientation of the Payloads on the Booster	23
5. Details of the Protuberances on the MOL, Configuration 42	24
6. Photographs of the Model at Various Stages of Assembly	
a. Sting Support System	25
b. Elastic Structure with Concentrated Weights. . .	25
c. Assembled Model.	25
7. Schematics of the Spring Support System	
a. Side View	26
b. Top View	26
8. Weight Distributions of the Model Components	
a. Core	27
b. SRM	28
c. Payloads	29
9. Details of the Forced-Oscillation Shaker System	
a. Installation Schematic.	30
b. Installation Photograph	31
10. Details of the Bending-Moment and Support Spring Force Sensors	32
11. Axial Locations of the Bending-Moment Sensors	33
12. Data Acquisition System.	34
13. Variation of Dynamic Pressure and Reynolds Number with Mach Number	
a. Dynamic Pressure	35
b. Reynolds Number.	35
14. Vector Representation of a Single-Degree-of-Freedom, Forced-Oscillation System with Viscous Damping . . .	36
15. Longitudinal Variation of the Normalized Modal Deflection for Configuration 42	
a. First Pitch Bending Mode, $f_0 = 17.87$	37
b. Second Pitch Bending Mode, $f_0 = 31.87$	37
16. Longitudinal Variation of the Normalized Modal Deflection for Configuration 43	
a. First Pitch Bending Mode, $f_0 = 20.03$	38
b. Second Pitch Bending Mode, $f_0 = 33.00$	38

<u>Figure</u>		<u>Page</u>
17.	Longitudinal Variation of the Normalized Modal Deflection for Configuration 44	
	a. First Pitch Bending Mode, $f_0 = 17.77$	39
	b. Second Pitch Bending Mode, $f_0 = 31.28$	39
18.	Longitudinal Variation of the Normalized Modal Deflection for Configuration 45	
	a. First Pitch Bending Mode, $f_0 = 16.43$	40
	b. Second Pitch Bending Mode, $f_0 = 30.65$	40
19.	Longitudinal Variation of the Normalized Modal Deflection for Configuration 46	
	a. First Pitch Bending Mode, $f_0 = 17.93$	41
	b. Second Pitch Bending Mode, $f_0 = 31.37$	41
20.	Effects of Nose Weight on Resonance Frequency	
	a. First Pitch Bending Mode	42
	b. Second Pitch Bending Mode	42
21.	Variation of the Total Acceleration and In-Phase Response with Frequency, Configuration 42, First Mode	
	a. Total Acceleration	43
	b. In-Phase Response	43
22.	Variation of the Total Acceleration and In-Phase Response with Frequency, Configuration 42, Second Mode	
	a. Total Acceleration	44
	b. In-Phase Response	44
23.	Variation of the Total Acceleration and In-Phase Response with Frequency, Configuration 43, First Mode	
	a. Total Acceleration	45
	b. In-Phase Response	45
24.	Variation of the Total Acceleration and In-Phase Response with Frequency, Configuration 43, Second Mode	
	a. Total Acceleration	46
	b. In-Phase Response	46
25.	Variation of the Total Acceleration and In-Phase Response with Frequency, Configuration 44, First Mode	
	a. Total Acceleration	47
	b. In-Phase Response	47

<u>Figure</u>	<u>Page</u>
26. Variation of the Total Acceleration and In-Phase Response with Frequency, Configuration 44, Second Mode	
a. Total Acceleration.	48
b. In-Phase Response	48
27. Variation of the Total Acceleration and In-Phase Response with Frequency, Configuration 45, First Mode	
a. Total Acceleration	49
b. In-Phase Response	49
28. Variation of the Total Acceleration and In-Phase Response with Frequency, Configuration 46, First Mode	
a. Total Acceleration.	50
b. In-Phase Response	50
29. Variations of the Total Elastic RMS Bending Moment with Mach Number	
a. Configuration 42.	51
b. Configuration 43.	51
c. Configuration 44.	51
d. Configuration 45.	52
e. Configuration 46.	52
30. Variations of Total Damping Coefficient with Mach Number, Configuration 42	
a. First Mode	53
b. Second Mode	53
31. Variations of Total Damping Coefficient with Mach Number, Configuration 43	
a. First Mode	54
b. Second Mode	54
32. Variations of Total Damping Coefficient with Mach Number, Configuration 44	
a. First Mode	55
b. Second Mode	55
33. Variation of Total Damping Coefficient with Mach Number, Configuration 45, First Mode	56
34. Variation of Total Damping Coefficient with Mach Number, Configuration 46, First Mode	56

	<u>Page</u>
II. DERIVATION OF MODEL SCALING PARAMETERS.	57
III. DERIVATION OF DAMPING PARAMETERS	60

NOMENCLATURE

\bar{A}	Acceleration amplitude, ft/sec ²
\bar{A}_I	Imaginary component of acceleration amplitude, ft/sec ²
\bar{A}_{Ig}	Imaginary component of the generalized acceleration amplitude, ft/sec ²
\bar{A}_R	Real component of acceleration amplitude, ft/sec ²
\bar{A}_{Rg}	Real component of the generalized acceleration amplitude, ft/sec ²
C	Total damping, lb-sec/ft
C_a	Aerodynamic damping, lb-sec/ft
C_{cr}	Critical damping, lb-sec/ft
C_s	Structural damping, lb-sec/ft
C. G.	Model station of the center of gravity, in.
d	Model core diameter, ft
\bar{F}	Exciting force amplitude, lb
\bar{F}_I	Imaginary component of exciting force amplitude, lb
\bar{F}_{Ig}	Imaginary component of the generalized exciting force amplitude, lb
\bar{F}_R	Real component of exciting force amplitude, lb
\bar{F}_{Rg}	Real component of the generalized exciting force amplitude, lb
f	Frequency, cps
f_a	Frequency of peak in-phase response above resonance, cps
f_b	Frequency of peak in-phase response below resonance, cps
f_o	Resonance frequency, cps
g	Total damping coefficient, $2(C_s + C_a)/C_{cr}$
g_s	Structural damping coefficient, $2C_s/C_{cr}$

$h(MS)$	Normalized modal displacement
$h(MS)_A$	Normalized modal displacement at model station -28.75
$h(MS)_F$	Normalized modal displacement at model station 105.0
K	Spring constant, lb/in.
M	Mass, lb-sec ² /ft
M_S	Generalized mass, lb-sec ² /ft
M_∞	Free-stream Mach number
MS	Model station, in.
p_∞	Free-stream static pressure, psf
q_∞	Free-stream dynamic pressure $0.7 p_\infty M_\infty^2$, psf
q_∞^N	Free-stream dynamic pressure corresponding to full-scale flight conditions, psf
R_I	Response in-phase with the exciting force, $(\bar{A} \cos \beta) / \bar{F}$, ft/lb-sec ²
Re_d	Reynolds number based on model core diameter, $V_\infty d / \nu_\infty$
V_∞	Free-stream velocity, ft/sec
W	Total model weight, lb
W_C	Weight of the model core, lb
W_M	Weight of the MOL, lb
W_N	Weight of the nose payloads, lb
W_S	Weight of each SRM, lb
w	Weight per unit length, lb/in.
\bar{X}	Model position amplitude, ft
β	Phase angle between the exciting force and the model position (see Fig. 14), deg
η	Phase angle of model position (see Fig. 14), deg
θ	Phase angle of the exciting force (see Fig. 14), deg
ν_∞	Kinematic viscosity of the free stream, ft ² /sec
σ_M	Total elastic rms bending moment, in.-lb
ϕ	Angular coordinate about the model, positive clockwise looking upstream with $\phi = 0$ at the top of the model, deg
ω	Circular frequency, rad/sec

TEST CONFIGURATIONS

<u>Configuration Number</u>	<u>Configuration Description</u>
42	Titan III, MOL with protuberances/Gemini, 7.5-segment SRM's
43	Titan III, MOL/unmanned Gemini, 7.5-segment SRM's
44	Titan III, MOL/Gemini, 7.5-segment SRM's
45	Titan III, MOL/SV-5, 7.5-segment SRM's
46	Titan III, MOL/standard fairing, 7.5-segment SRM's

SECTION I INTRODUCTION

Aeroelastic modeling techniques have been applied to a 0.07-scale model of the Titan III launch vehicle, and a wind tunnel investigation has been initiated to evaluate the structural response of various configurations at transonic speeds. During previous tests (see Ref. 1) a number of payload and booster combinations were tested to measure the bending-moment distribution over the model resulting from buffet air loads. The last of these tunnel entries was the first of several entries planned under the Phase III Wind Tunnel Test Plan. As a continuation of this test plan, the present investigation was conducted to measure the structural and aerodynamic damping characteristics of various Titan III/MOL configurations by the forced-oscillation technique. The present configurations were either the same as or similar to those tested during the buffet response entry. In addition to the damping measurements, the buffet bending moments were recorded during the present entry for comparison with previous data. The test was conducted in the Propulsion Wind Tunnel, Transonic (16T) at AEDC during the period from April 27 through May 19, 1967.

SECTION II APPARATUS

2.1 TEST FACILITY

Tunnel 16T is a variable density wind tunnel. The test section is 16 ft square and is lined with perforated plates to allow continuous operation through the Mach number range from 0.55 to 1.60 with minimum wall interference.

Details of the test section showing the location of the test article and the support strut arrangement are presented in Fig. 1. Photographs of the various configurations as installed in the test section are presented in Fig. 2. A more extensive description of the tunnel is given in Ref. 2, and the latest calibration results are presented in Refs. 3 and 4.

2.2 TEST ARTICLE

2.2.1 General

The basic test article was a 0.07-scaled aeroelastic model of a Titan III launch vehicle with payloads consisting of the MOL in combination

with various nose configurations. The model booster was the same as tested during the previous Phase III test program (Ref. 1) and consisted of a modified Titan III core centerbody and two 7.5-segment strap-on, solid-rocket motors (SRM). The full-scale diameters of the core and SRM's are 120 and 121 in., respectively. Geometric details of the model booster are presented in Fig. 3. A summary of the various configurations tested and corresponding configuration numbers are presented in the nomenclature. Geometric details of the payloads are presented in Fig. 4. In general, the reaction control rockets were the only protuberances external to the MOL section; however, one configuration (42) was tested with five additional protuberances, as illustrated in Fig. 5.

The model physical properties are presented in Table I, and a derivation of the model scale factors is presented in Appendix II.

2.2.2 Model and Sting Support System Construction

Some of the details of the model and sting support system construction are shown in photographs of the model at various stages of the assembly in Fig. 6. The sting support system consisted of three steel pipes cantilevered from a cross member which attached to the PWT sting system (Fig. 6a). The long center prong entered the model core, and the shorter outside prongs entered the SRM's. The model was supported on the sting by spring systems housed inside the sting as shown in side and top view schematics of the spring support system in Fig. 7. The spring support system was designed to restrain the model in the axial direction, to support the model weight, and to provide a minimum of restraint to motion in the pitch and yaw free-free bending modes (see Ref. 1). The model was supported at three points - at the upstream end of the core and at the downstream end of each SRM. Positioning and braking systems for the model are described in Ref. 1.

The structural backbone of the model was the core, SRM, and MOL elastic structure. The core structure was constructed of 2024-T4 aluminum tubing, and the SRM structures were constructed of 6061-T6 aluminum tubing. The tubes were machined to satisfy the scale stiffness requirements. Steel weights were attached to the elastic structures to simulate the running inertia and mass characteristics. The weight distributions for the core and SRM's are presented in Figs. 8a and b, respectively. The correct aerodynamic form for the core and SRM's was obtained by covering the skeletal structures with aluminum cylindrical

TABLE I
SUMMARY OF MODEL PHYSICAL PROPERTIES

Physical Property		Config. 42		Config. 43		Config. 44		Config. 45		Config. 46	
		Free-Free Pitch Bonding Modes									
		First	Second	First	Second	First	Second	First	Second	First	Second
t _o	Experimental	17.87	31.87	20.03	33.00	17.77	31.28	16.43	30.65	17.93	31.37
	Design	18.50	31.50	19.50	31.60	18.50	31.50	16.50	29.60	---	---
g _s	Experimental	0.018	0.012	0.018	0.013	0.019	0.011	0.020	---	0.018	---
	Design	0.035	0.010	0.035	0.010	0.035	0.010	0.035	0.010	---	---
w _T	Experimental	453.7		451.7		453.6		454.3		453.7	
	Design	456.4		454.5		456.4		456.3		---	
w _N	Experimental	2.8		0.9		2.8		3.5		2.9	
CG	Experimental	55.5		55.9		55.5		55.3		55.5	

Note: Weight represents $M_{cw} = 1.0$ condition.

segments. The joints between the aluminum segments were sealed with a silastic rubber which enabled the segments to move independently and thus not restrain the model in bending. The MOL section was constructed of 7075-T6 aluminum tubing and chemically milled to obtain the correct scaled stiffness distribution. The MOL weight distribution is presented in Fig. 8c. Balsa wood was bonded directly to the MOL aluminum structure and shaped to the correct aerodynamic geometry.

The various nose payloads were constructed of a skeleton of aluminum and/or plywood with the external contour shaped from balsa wood. The nose payload weight, center of gravity, and mass moment of inertia were simulated; however, the stiffness was higher than that dictated by similitude laws. The weight distributions of the various nose payloads are presented in Fig. 8c.

2.2.3 Excitation System

A single electromagnetic shaker was used to excite the model in its pitch bending modes. The shaker was mounted below and aft of the model as shown in Fig. 9. The model was excited through a semirigid beam (natural frequency of 250 cps) which was cantilevered from the base of the model. The free end of the beam was connected to the shaker through a drive rod. Universal joints in the drive rod permitted lateral motion of the model. The housing for the shaker drive system was mounted directly to the sting support cross member. Fouling sensors and mechanical stops were also attached to the shaker drive housing to provide a means of limiting the shaker force to the model should the shaker become uncontrollable.

2.3 INSTRUMENTATION

2.3.1 Model

Instrumentation in the model consisted of the following:

1. Pitch and yaw bending-moment sensors located on the core and MOL structures.
2. Normal- and side-force sensors located on the support springs.
3. Pitch and yaw accelerometers located in the upstream end of the MOL payload. Pitch accelerometers located in the aft end of the core.

4. Position sensor located at the forward support spring attachment point.
5. Force sensor located between the shaker arm and the shaker drive rod.

The bending-moment and force sensors were strain-gage bridges with four active arms. The gages of the bending-moment sensors were bonded to the exterior of the core and MOL structures such that the geometric centers of the sensors were at the model centerlines. The gages of the force sensors were similarly installed on the support springs. Typical core and spring cross sections showing details of the gage installations are presented in Fig. 10. Axial locations of the bending-moment sensors are presented in Fig. 11.

Two crystal accelerometers were installed in the MOL payload at model station -28.75. The accelerometers were oriented such that one was sensitive to motion in the pitch plane, and the other sensitive to motion in the yaw plane. Two other accelerometers were located in the aft end of the core at model station 88.00. Both accelerometers were sensitive to motion in the pitch plane.

The position sensor was a linear differential transformer that measured the vertical displacement of the model from the center of the sting support.

The force input to the model from the electromagnetic shaker was measured by a crystal-type load cell. The load cell was located between the shaker drive rod and the shaker arm which was cantilevered from the base of the model core (see Fig. 9a). The load cell output signal was used in conjunction with the pitch accelerometer in the MOL payload to determine the aerodynamic damping by means of an electronic component analyzer.

2.3.2 Data Recording and Monitoring

Outputs from the model instrumentation were conditioned and recorded and/or monitored on-line as illustrated in Fig. 12. Dynamic measurements were recorded on a 14-channel magnetic tape recorder and two oscillographs. Up to 4-rms voltmeters with integrating circuits for time averaging the fluctuating rms signals were used to obtain on-line readings of the bending-moment sensor outputs. A waveform analyzer was used as a control and readout system for the forced-oscillation phases of the test. A variable frequency oscillator, which was an integral part of the analyzer, was connected to the electromagnetic shaker and provided control

of the frequency and amplitude of the exciting force to the model. The shaker force sensor output and the output of the pitch accelerometer in the MOL payload were connected to the two input channels of the analyzer. The analyzer, using sine and cosine reference signals from the oscillator, evaluated the force and acceleration signals by Fourier analysis methods and provided over 40 db of noise and harmonic rejection. The following parameters were resolved by the analyzer (where real and imaginary components are relative to the oscillator signal and in-phase and quadrature components are relative to the exciting force):

1. Frequency
2. Force, real component
3. Force, imaginary component
4. Force, total
5. Acceleration, real component
6. Acceleration, imaginary component
7. Acceleration, total
8. Acceleration, in-phase
9. Acceleration, quadrature
10. Phase angle of force relative to oscillator signal
11. Phase angle of acceleration relative to oscillator signal
12. Phase angle between force and acceleration
13. Response, in-phase, defined as ratio of in-phase acceleration to total force
14. Response, quadrature, defined as ratio of quadrature acceleration to total force
15. Response, total, defined as ratio of total acceleration to total force

The analyzer also provided for averaging the foregoing parameters at time intervals ranging from 0.01 to 50 sec. All steady-state forced-oscillation data were obtained using the 50-sec time constant. Although all of the 15 parameters were available from the analyzer, only items 1, 2, 3, 5, and 6 were recorded on line. These parameters, which were in the form of d-c voltages, were processed through the PWT force and moment readout system (Famros) described in Ref. 2. Other steady-state measurements were also processed through the Famros system.

All the model instrumentation except the position sensor was connected through a channel selector panel so that the outputs could be monitored on rms voltmeters and/or oscilloscopes. A schlieren system and television cameras were also used to monitor the model during the test.

SECTION III TEST DESCRIPTION

3.1 TEST CONDITIONS

The test was conducted in the Mach number range from 0.80 to 1.10 and at zero angle of attack. To satisfy model scaling parameters (see Appendix II), it was desirable to test at dynamic pressures corresponding to the full-scale flight trajectories. However, the buffet loads on the model at the flight dynamic pressures imposed stresses on the model approaching the design limit. Thus, to excite the model above the level of the buffet response as required for the aerodynamic damping study, it was necessary to test at reduced dynamic pressure levels. These levels ranged from 50 to 85 percent of the flight dynamic pressures. Variations of the dynamic pressure (q_∞) with Mach number (M_∞) for the various dynamic pressure schedules of the test are presented in Fig. 13a. The dynamic pressure variation noted as $q_\infty = 1.0 q_{\infty N}$ represents the upper limit of the q_∞ dispersion for the full-scale flight trajectory. The variation of Reynolds number, based on the model core diameter, with Mach number for the range of dynamic pressure of the test is presented in Fig. 13b. It should be pointed out that Reynolds numbers for the model and prototype vehicle do not match (see Appendix II). This mismatch was not considered detrimental to the purpose of the test.

3.2 TEST PROCEDURE

The test consisted of two distinct phases: (1) air-off model vibration testing, and (2) air-on buffet response and model vibration testing. These phases are discussed separately.

3.2.1 Air-Off Model Vibration Testing

With the model mounted in the tunnel and no air flowing, the model was excited by the electromagnetic shaker to establish the modal

characteristics of the various configurations in the pitch plane when supported by the model sting system and the remaining PWT sting assembly. These tests were normally conducted at three amplitudes of excitation (corresponding to the amplitudes of the air-on vibration tests) and before and after an air-on-run. Generally, the following procedure was followed:

1. Excitation was applied to the aft end of the core by the electromagnetic shaker and the desired pitch bending mode was "tuned" by varying the frequency of the control oscillator. The resonance condition was indicated by the change in phase of the response when the exciting frequency passed through resonance. The change in phase was easily detectable from the in-phase response as displayed directly on the waveform analyzer by a direct-current voltmeter with a center zero. The in-phase response peaks at frequencies just below and just above resonance and is zero at the resonance frequency. Thus, tuning to the resonance frequency involved nulling the in-phase response voltmeter to zero.
2. After each mode was properly tuned and the amplitude of excitation set, the experimental mode shapes were determined by measuring the variation along the model of the quadrature acceleration ($\bar{A} \sin \beta$) of the model by means of a roving accelerometer. It was pointed out in Refs. 5 and 6 that the phase separation technique, whereby the mode shape is defined in terms of the quadrature acceleration rather than the total acceleration, greatly increases the accuracy of the mode shape. The mode shapes were normalized to the quadrature acceleration at model station -32.00.
3. After each modal survey, up to 20 data points were recorded through the on-line data acquisition system and on-line computation, and tabulation of the forced oscillation parameters were obtained. Also, the outputs of the various sensors were recorded on magnetic tape and on the oscillographs.
4. The damping of each elastic mode was then recorded on an oscillograph by instantaneously removing the excitation force and allowing the model to freely decay.
5. The variation with frequency of the in-phase response and the total acceleration were obtained utilizing two x-y plotters on the analyzer. These plots ranged from approximately 2 cps below resonance to approximately 2 cps above resonance.

3.2.2 Air-On Buffet Response and Model Vibration Testing

After the air-off data were obtained, the tunnel was started at a low dynamic pressure. The model was free to respond to the airflow as dynamic pressure was increased until the desired test conditions were realized. All bending-moment and force sensors were monitored to ensure that loads in excess of the structural capability of the model were not reached. Excessive loads were not encountered during the present test, and it was not necessary to use the snubber and brake systems discussed in Ref. 1. At each test condition, the buffet response measurements were obtained by allowing the model to freely respond to the flow conditions, while approximately 2 min of magnetic tape data were recorded. During this time, on-line rms values of selected bending-moment sensor outputs were hand recorded.

After the buffet response data were obtained, the model was forced to vibrate at resonance in the desired pitch free-free bending mode. It was noted that the excitation force had to be sufficiently large to excite the model above the level of the buffet forces in order to obtain a well defined resonance condition. Resonance was tuned in approximately the same manner as discussed in step 1 of Section 3.2.1. Approximately 2 min of constant amplitude and frequency forced-oscillation data were recorded on magnetic tape and approximately 20 data points of steady-state measurements were recorded through the data acquisition system. After the forced-oscillation data at resonance were obtained, the variations of the excitation force and acceleration response with frequency were recorded on magnetic tape. These data were obtained by sweeping the frequency range from approximately 2 cps below to 2 cps above the resonance frequency using the automatic frequency scan capability of the control oscillator. The variation with frequency of the in-phase response and the total acceleration were plotted using the two x-y plotters on the analyzer. The plots were obtained concurrently with the recording of the sweep data on tape. This procedure was repeated for each mode and amplitude of excitation. The air-on decaying oscillations did not produce a signal that was clean enough to permit the use of the logarithmic decrement method for determining damping. Therefore, free decays were not recorded for air-on conditions.

3.3 DATA REDUCTION

Steady-state force and bending-moment measurements obtained from the support-spring and core instrumentation, respectively, were reduced and tabulated on-line. These data were used primarily to monitor the test and are not presented herein.

The buffet response bending-moment measurements as recorded on magnetic tape will be reduced by the Martin-Marietta Corporation, Denver Division. Selected rms bending-moment data were hand re-recorded during the test, and these data are presented herein. The rms data were obtained using time-integrating rms voltmeter systems. The real time data sample for the rms analysis was 50 sec.

The damping measurements were obtained on-line utilizing the waveform analyzer described in Section 2.3.2. The analyzer resolved the exciting force and the resulting model acceleration into real and imaginary components. These components, together with the circular frequency, define the damping for each elastic mode as follows:

$$C = \omega \left(\frac{\bar{F}_R \bar{A}_I - \bar{F}_I \bar{A}_R}{\bar{A}_R^2 - \bar{A}_I^2} \right) h(MS)_F h(MS)_A \quad (1)$$

A vector representation of these components is presented in Fig. 14, and a derivation of the damping equation is presented in Appendix III. The structural damping was determined by exciting the model at air-off conditions and is presented in terms of the structural damping coefficient. For small structural damping the coefficient may be expressed as:

$$g_s = 2 \frac{C_s}{C_{cr}} = 2 \frac{C}{C_{cr}} \bigg|_{\text{air-off}} \quad (2)$$

The damping given by Eq. (1) for air-on conditions is the sum of the structural and aerodynamic damping terms. The aerodynamic damping is presented in terms of the total damping coefficient:

$$g = 2 \frac{(C_s + C_a)}{C_{cr}} = 2 \frac{C}{C_{cr}} \bigg|_{\text{air-on}} \quad (3)$$

Since Eq. (1) defines an absolute value of the damping rather than a damping ratio, it was necessary to determine the critical damping for use in Eqs. (2) and (3). The critical damping was derived by comparing the measured air-off damping from Eq. (1) with the damping ratio as determined by the logarithmic decrement method from the air-off free-oscillation decays. The critical damping was also determined using values of the generalized masses from the following equation:

$$C_{cr} = 2\omega M_s$$

where the generalized masses were experimentally determined by the incremental mass method (Ref. 7). However, critical damping determined by this method was not felt to be as accurate as that defined by the free-oscillation decay for determining the damping coefficient (see Section 4.1.2).

SECTION IV

RESULTS AND DISCUSSION

It was noted in Section 3.2 that the test was conducted in two distinct phases: (1) air-off vibration testing and (2) air-on buffet response and vibration testing. The results of these phases of the test are discussed separately.

4.1 AIR-OFF VIBRATION TESTING

Air-off vibration of the model was conducted to evaluate the modal characteristics of the various configurations in the pitch plane. The following parameters, which may be interpreted as defining the elastic properties of the model, were determined for the first and second pitch bending modes: (1) mode shapes, (2) resonant frequencies, and (3) structural damping. It was discovered during the air-off vibration testing that significant pitch-yaw coupling occurred in the first mode for certain configurations. To show the effects of the coupling, the variation with frequency of the in-phase response and the total acceleration were also recorded for all configurations.

4.1.1 Model Elastic Properties

Longitudinal variations of the normalized amplitudes, $h(MS)$, of the first and second pitch bending modes are presented for the various configurations in Figs. 15 through 19. All configurations exhibited similar mode shapes. The flexural stiffness of the core is significantly less than that of the SRM's as indicated by the larger variation of the core deflection. For the first mode the SRM's were essentially rigid bodies experiencing pitch motion, whereas, some bending can be detected in the second mode. It is interesting to note that the payload weight had a significant effect on the core deflection for the second mode. The variation of the core deflection for configuration 43 with a payload of 0.9 lb was considerably less than that of configuration 45 with a payload weight of 3.5 lb.

Significant changes in frequency also resulted from payload weight changes as shown in Fig. 20. Increasing the payload weight decreased the resonance frequency of both the first and second pitch bending modes.

Structural damping of the various configurations was determined as discussed in Sections 3.2 and 3.3 and Appendix III. Some variation in damping with excitation force was observed; however, this variation was

generally within the scatter of the data. A summary of the structural damping coefficients (g_s) together with other model physical properties is presented in Table I. Damping coefficients presented in the table represent average values. It should be noted that the model structural damping coefficient for the first pitch bending mode ranged from 50 to 60 percent of that estimated for the prototype vehicle. This indicates that the model was conservative since it should be more responsive to buffet loads than the prototype vehicle.

4.1.2 Forced-Oscillation Response Characteristics

Response characteristics of the various configurations are exhibited by variations with frequency of the total acceleration (\bar{A}) and the in-phase response (R_I) as shown in Figs. 21 through 28. For certain configurations, significant coupling between the pitch bending modes and the yaw bending modes and/or sting vibration was encountered. One example is shown for the first pitch bending mode of configuration 42, Fig. 21a. Coupling is evidenced by the small secondary peaks in \bar{A} and R_I which occur at frequencies below and above the resonance frequency. The effect of the coupling is to decrease the pitch acceleration in the neighborhood of the resonance frequency, and thus cause the total response (\bar{A}/\bar{F}) to be less than the value which would occur for pitch plane vibrations alone. Since damping is inversely proportional to the response, the indicated damping is too large. Coupling was not present in the second pitch bending mode of configuration 42 as evidenced by the smooth variation of \bar{A} and R_I with frequency and the single peak in \bar{A} at the resonance frequency, Fig. 22. Configuration 43 also experienced significant coupling in the first pitch bending mode as shown by the solid curves in Fig. 23. This coupling resulted primarily from sting vibration. A sting extension, which supports the payload nose brake, was removed and most of the coupling was eliminated as shown by the broken curves in Fig. 23. Also, the resonance frequency was lower for the configuration without the sting extension. Some coupling remained (probably with the first yaw bending mode) since \bar{A} peaked at a frequency slightly above the resonance frequency. Similar variations of \bar{A} and R_I with frequency for other configurations show only small coupling effects.

It was not possible to estimate the reduction in measured damping values resulting from the coupling although the error was partly reduced by accounting for the coupling in evaluating critical damping (C_{cr}). This was accomplished by determining C_{cr} as follows:

$$C_{cr} = 2C/g_s$$

where g_s is the structural damping coefficient as determined from free decays and C is the structural damping obtained from forced oscillation.

The result is that C_{cr} is adjusted for the coupling in an amount proportional to the coupling effect on C such that the ratio C/C_{cr} is approximately correct.

4.2 BUFFET RESPONSE

Variations with free-stream Mach number of the total elastic rms bending moment resulting from the structural response of the model in the pitch free-free bending modes to buffet airloads are presented in Fig. 29. These results were obtained by hand recording rms voltages of a selected bending-moment sensor output during the test. The sensor at model station 35.48 was selected because of its close proximity to the station of peak bending-moment sensitivity in the first and second pitch bending modes. Also, it should be noted that the bending-moment sensor outputs were filtered below 10 cps to exclude the rigid body frequencies of the support springs from the rms analysis. A discussion of the effects of the support springs is presented in Ref. 1. Since the present test was generally conducted at dynamic pressures below the Ref. 1 test, it was necessary to adjust the bending-moment data so that a comparison of the two test results could be made. An analysis of the effects of dynamic pressure was made in Ref. 1, and it was shown that the bending-moment response was proportional to the dynamic pressure. Therefore, the

variations of $\sigma_M \left(\frac{q_\infty N}{q_\infty} \right)$ with M_∞ from the present bending-moment data are

compared with the data from Ref. 1 for similar configurations. Considering that minor changes had been made to the weight distributions and that the flow field about the model may have been slightly altered because of the presence of the excitation system, the results compare reasonably well. The peak buffet response occurred near $M_\infty = 0.95$ for all configurations. The external geometries of configurations 43, 44, and 45 were the same as configurations 32, 41, and 34, respectively, in Ref. 1. The protuberances on the MOL differed between configuration 42 of the present test and configuration 31 in Ref. 1; however, both sets of protuberances appeared to have similar effects on the buffet response (Fig. 29a). Configuration 46 was not tested previously, and a comparison of the results cannot be made.

4.3 AIR-ON VIBRATION TESTING

Air-on vibration testing was conducted to measure the total damping (combined structural and aerodynamic damping) by the forced-oscillation technique. Variations of the total damping coefficient (g) with Mach number (M_∞) are presented in Figs. 30 through 34. The structural damping

coefficients (g_s) as determined from air-off vibration testing are also presented in Figs. 30 through 34. The dispersions of g_s resulting from exciting force amplitude, temperature, and other factors are represented by the cross-hatched band. The aerodynamic damping coefficient (C_a/C_{cr}) is a function of the total damping (g) and the structural damping (g_s):

$$\frac{C_a}{C_{cr}} = \frac{g - g_s}{2}$$

The Gemini configurations (configurations 42, 43, and 44) exhibited similar damping characteristics for the first pitch bending mode, Figs. 30a, 31a, and 32a. The aerodynamic damping was relatively low at the lower Mach numbers and increased rapidly in the Mach number range from 0.925 to 1.00. Peak buffet response also occurs in this Mach number range. The variations of aerodynamic damping for the second pitch bending mode with Mach number (configurations 42, 43, and 44, Figs. 30b, 31b, and 32b) were less than those observed for the first mode. For configuration 43, the aerodynamic damping was approximately zero. The effect of dynamic pressure on aerodynamic damping was similar for configurations 42 and 44. As dynamic pressure was increased, the aerodynamic damping also increased; although the increase in damping was not necessarily proportional to dynamic pressure for all Mach numbers. For configuration 43, it should be noted that the damping data for the first mode are for the configuration without the sting extension (see Section 4.1). For this configuration, data were obtained only for $q_\infty = 0.50 q_{\infty N}$. The effect of dynamic pressure on the damping for the second mode of configuration 43 was negligible, as may be expected since the aerodynamic damping was approximately zero.

The SV-5 configuration and the standard fairing configuration (configurations 45 and 46, respectively) were tested for aerodynamic damping only in the first pitch bending mode, and the results are presented in Figs. 33 and 34. The aerodynamic damping for configuration 45 increased almost monotonically from 0.85 to 1.10. For configuration 46, the aerodynamic damping increased rapidly from 0.925 to 0.975, peaked at 0.975, and decreased from 0.975 to 1.00. The effect of increasing dynamic pressure was to increase the aerodynamic damping as observed for configurations 42 and 44.

The response characteristics of the various configurations were also recorded for air-on conditions as plots of \bar{A} and R_I versus frequency. The results were similar to those for air-off conditions (see Section 4.1); however, the air-on data were somewhat ill-defined

because of the presence of nonstationary, random buffet forces. The coupling effects, noted in the air-off data for configurations 42 and 43, were also present for air-on conditions.

SECTION V CONCLUSIONS

On the basis of a wind tunnel test conducted on aeroelastically scaled Titan III/MOL configurations, the following conclusions can be drawn:

1. All configurations experienced peak buffet response near Mach number 0.95. The buffet response for the Gemini and SV-5 configurations agreed reasonably well with previous test results for the same or similar configurations.
2. The model structural damping for the first pitch bending mode ranged from 50 to 60 percent of that estimated for the prototype vehicle. Thus, buffet response measurements should be conservative for estimating the full-scale buffet response.
3. Significant coupling between the pitch bending modes and the yaw bending modes and/or sting vibration was noted in both the air-off and air-on vibration data. This problem which affects the damping results could only be approximately resolved.
4. The aerodynamic damping was generally positive and varied with Mach number. The largest variations occurred in the Mach number range from 0.925 to 1.00 for the Gemini and SV-5 configurations.
5. Increasing dynamic pressure caused an increase in aerodynamic damping, although the increase in damping was not necessarily proportional to dynamic pressure.

REFERENCES

1. Robertson, J. E. and Brice, T. R. "Buffet Response of Aero-elastically Scaled Titan III Missile Configurations at Transonic Mach Numbers." AEDC-TR-67-33 (AD808700), March 1967.
2. Test Facilities Handbook (6th Edition). "Propulsion Wind Tunnel Facility, Vol. 5." Arnold Engineering Development Center, November 1966.
3. Chevalier, H. L. "Calibration of the 16-Foot Transonic Circuit with a Modified Model Support System and Test Section." AEDC-TN-60-164 (AD241785), August 1960.
4. Riddle, C. D. "An Investigation of Free-Stream Fluctuating Pressures in the 16-Foot Tunnels of the Propulsion Wind Tunnel Facility." AEDC-TR-67-167, August 1967.
5. Stahle, C. V. "A Phase Separation Technique for the Experimental Determination of Normal Vibration Modes of Flight Vehicles." Paper Presented at the "29th Symposium on Shock, Vibration, and Associated Environments." San Francisco, California, November 1960.
6. Stahle, C. V., Jr. "Phase Separation Technique for Ground Vibration Testing." Aerospace Engineering, July 1962.
7. Mazet, R. "Some Aspects of Ground and Flight Vibration Tests." AGARD Report 40-T, April 1956.
8. Pre-Test Report on 7% Transonic Buffet for Various Titan III Configurations. Martin-Marietta Corporation, Denver Division, Martin-Denver SSD-CR-65-257, January 1956.

APPENDIXES

- I. ILLUSTRATIONS**
- II. DERIVATION OF MODEL SCALING PARAMETERS**
- III. DERIVATION OF DAMPING PARAMETERS**

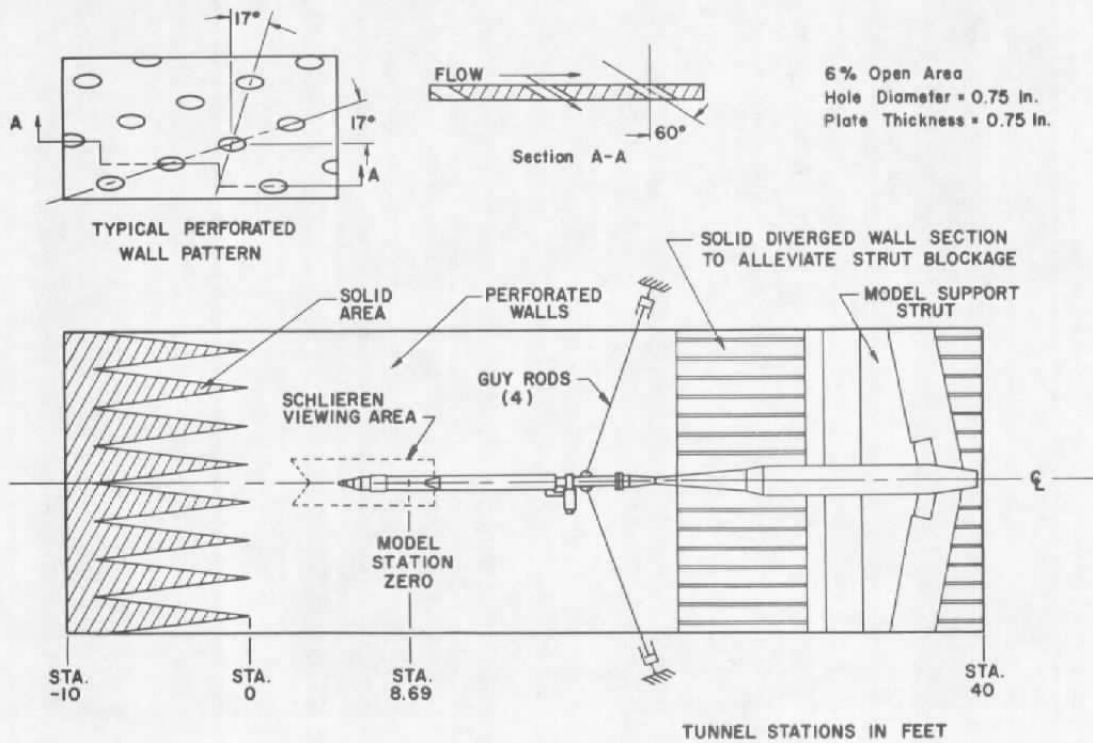
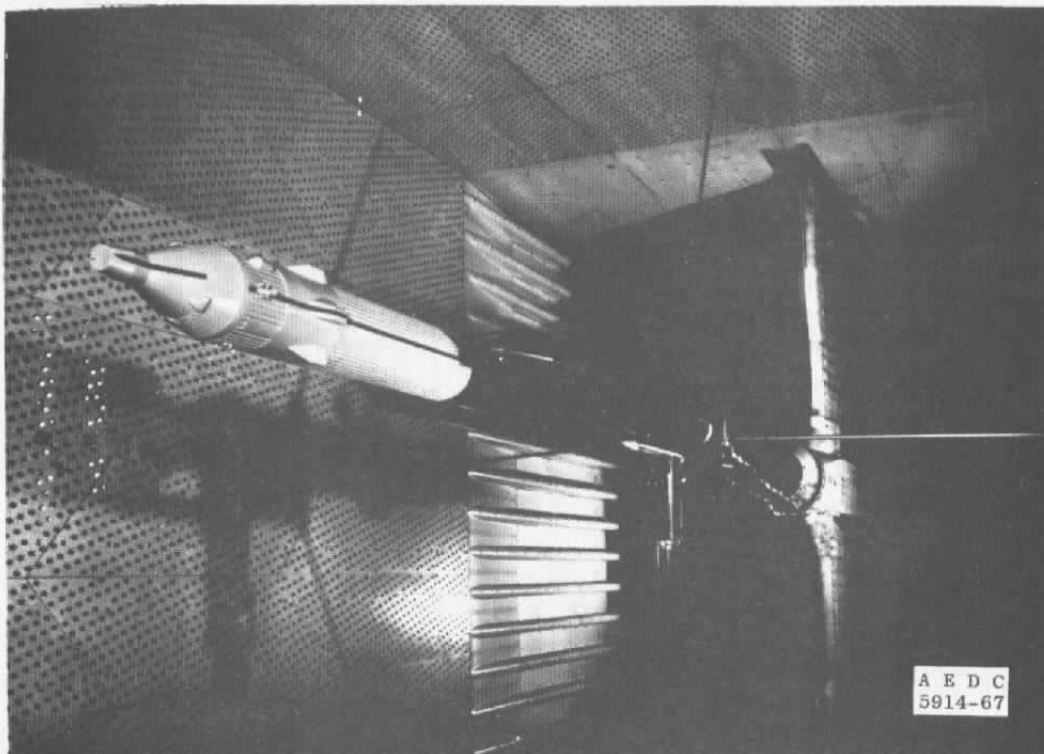
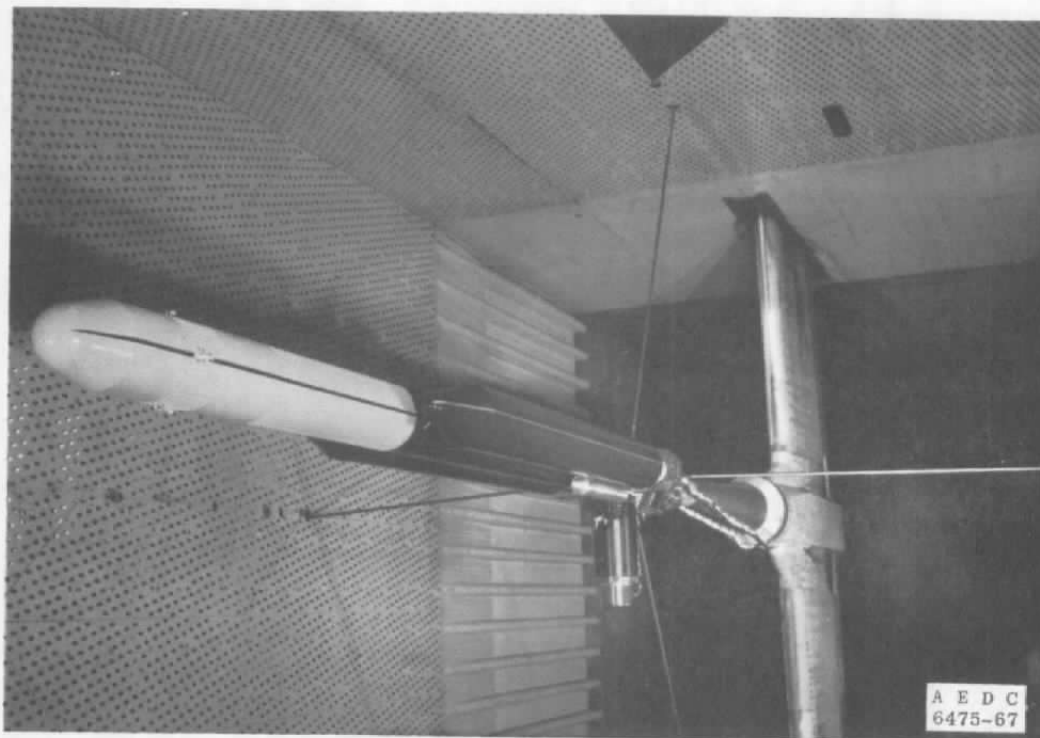


Fig. 1 Schematic of the Model Installation in Tunnel 16T

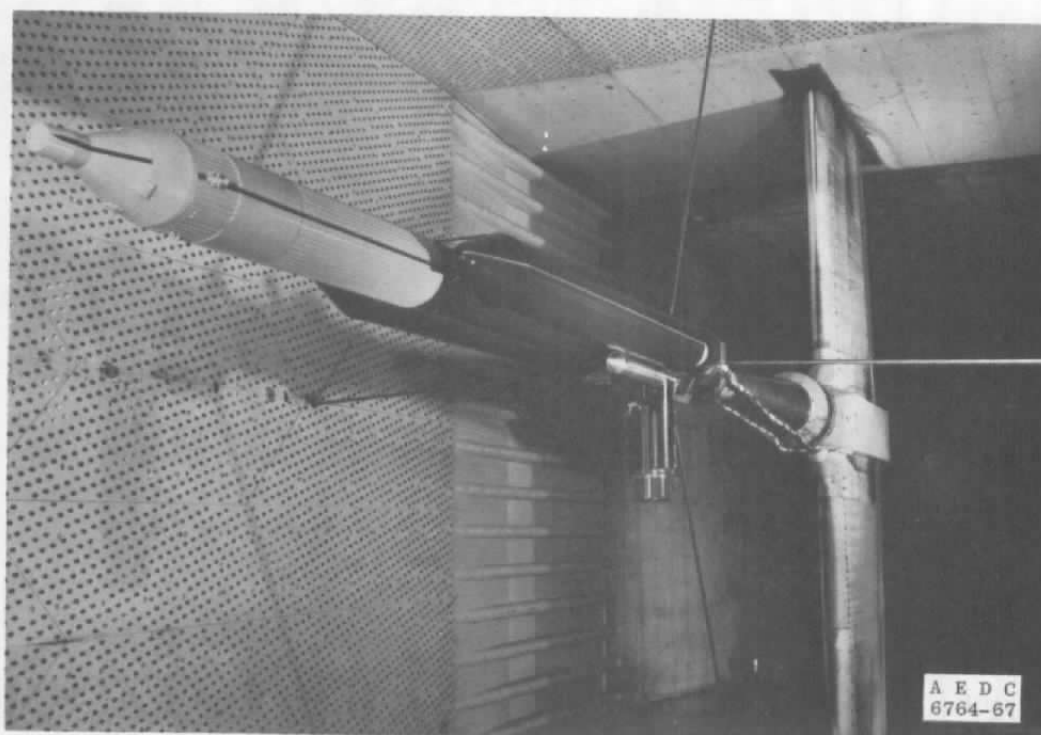


a. Configuration 42

Fig. 2 Photographs of the Various Configurations Installed in Tunnel 16T

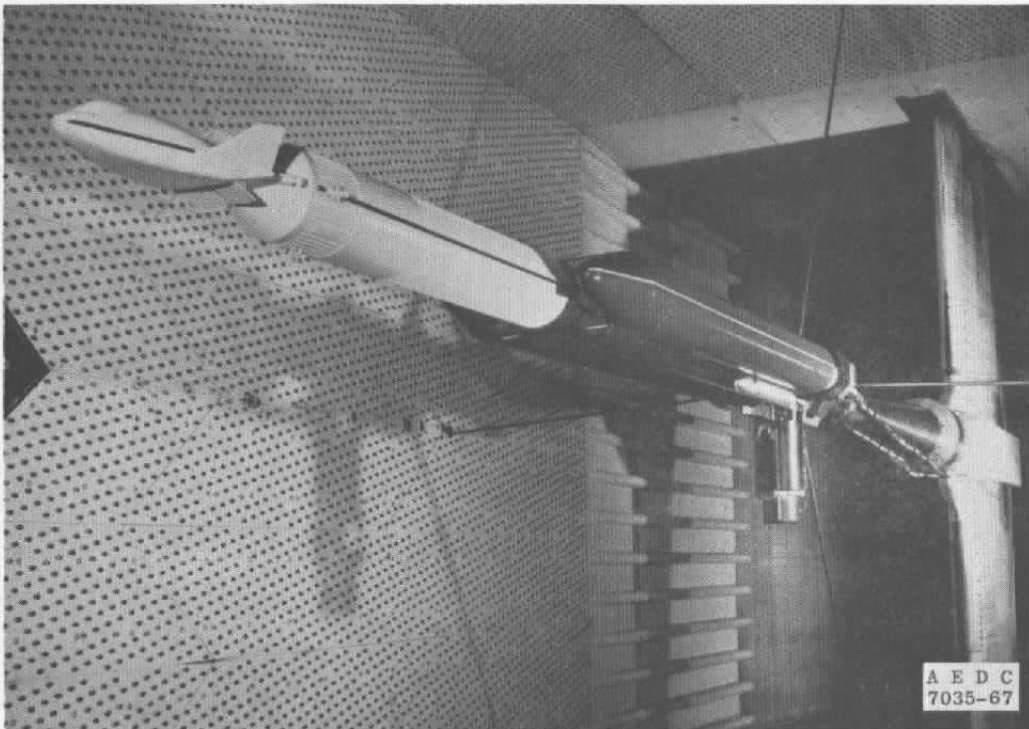


b. Configuration 43

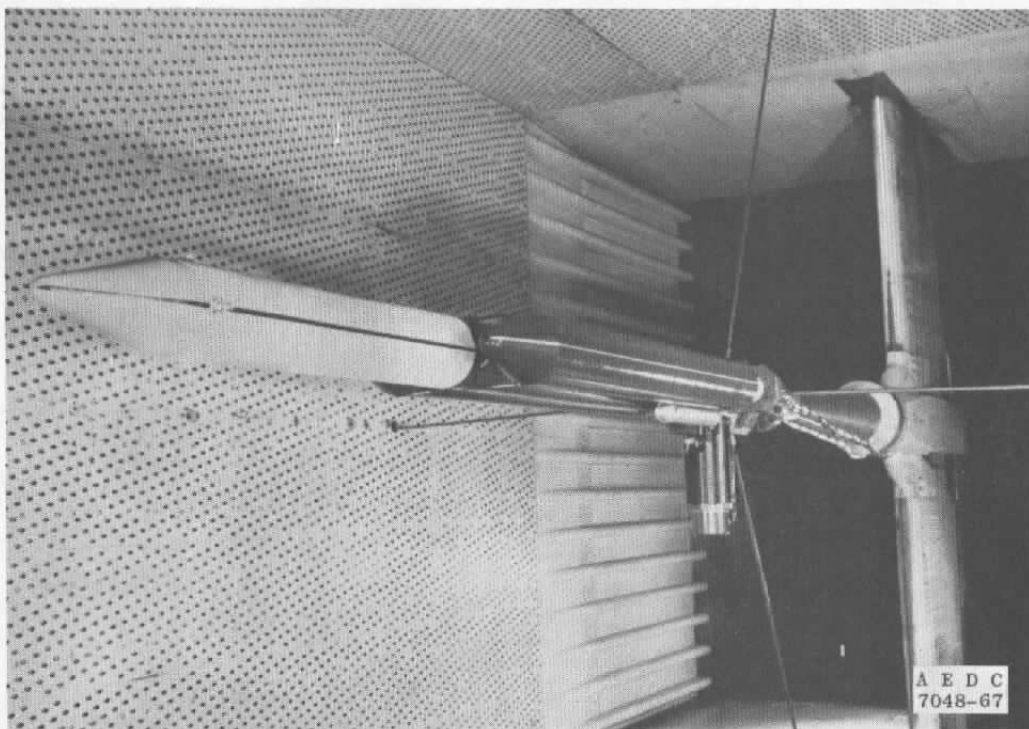


c. Configuration 44

Fig. 2 Continued



d. Configuration 45



e. Configuration 46

Fig. 2 Concluded

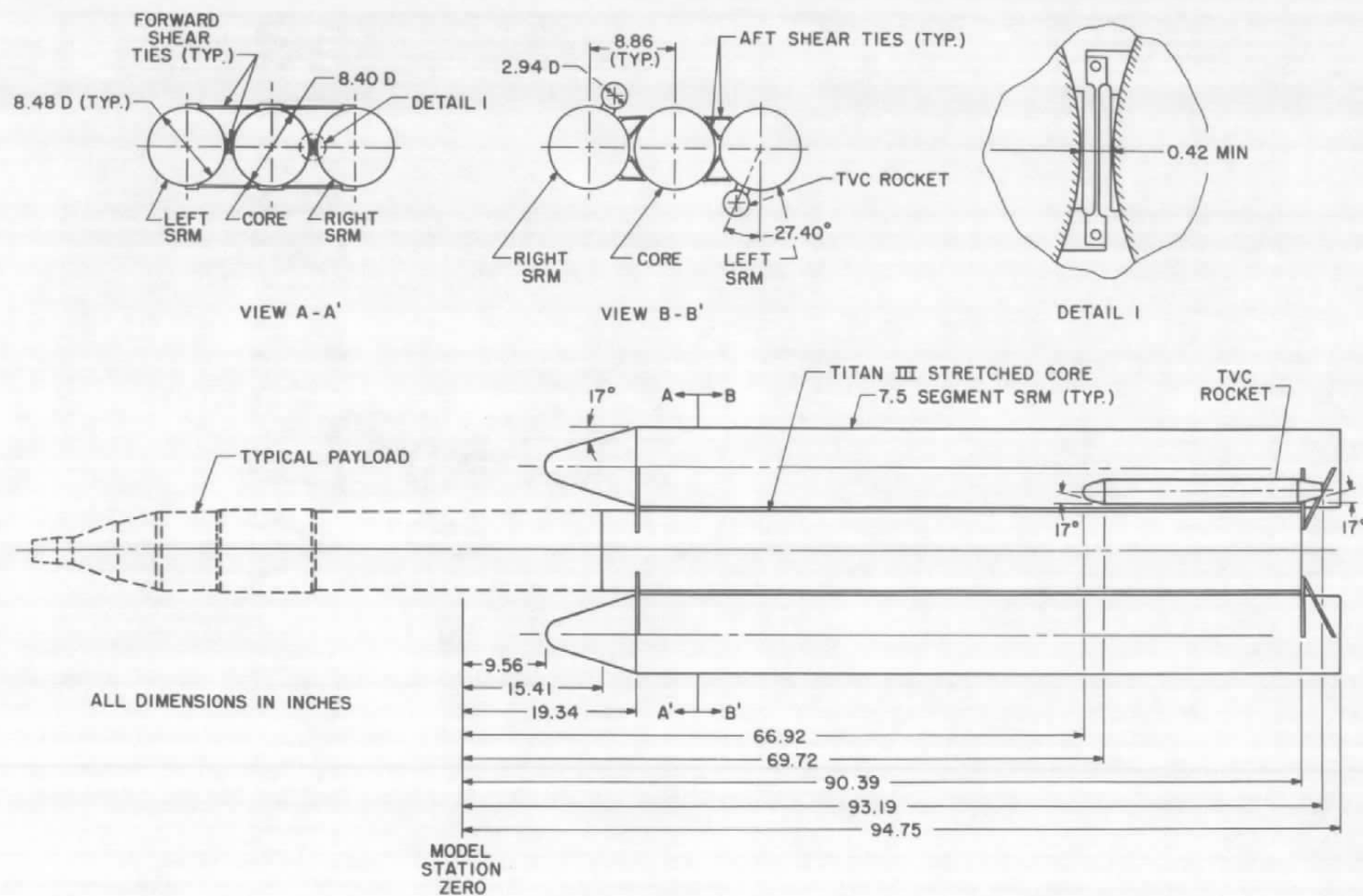


Fig. 3 Details of the Titan III Booster

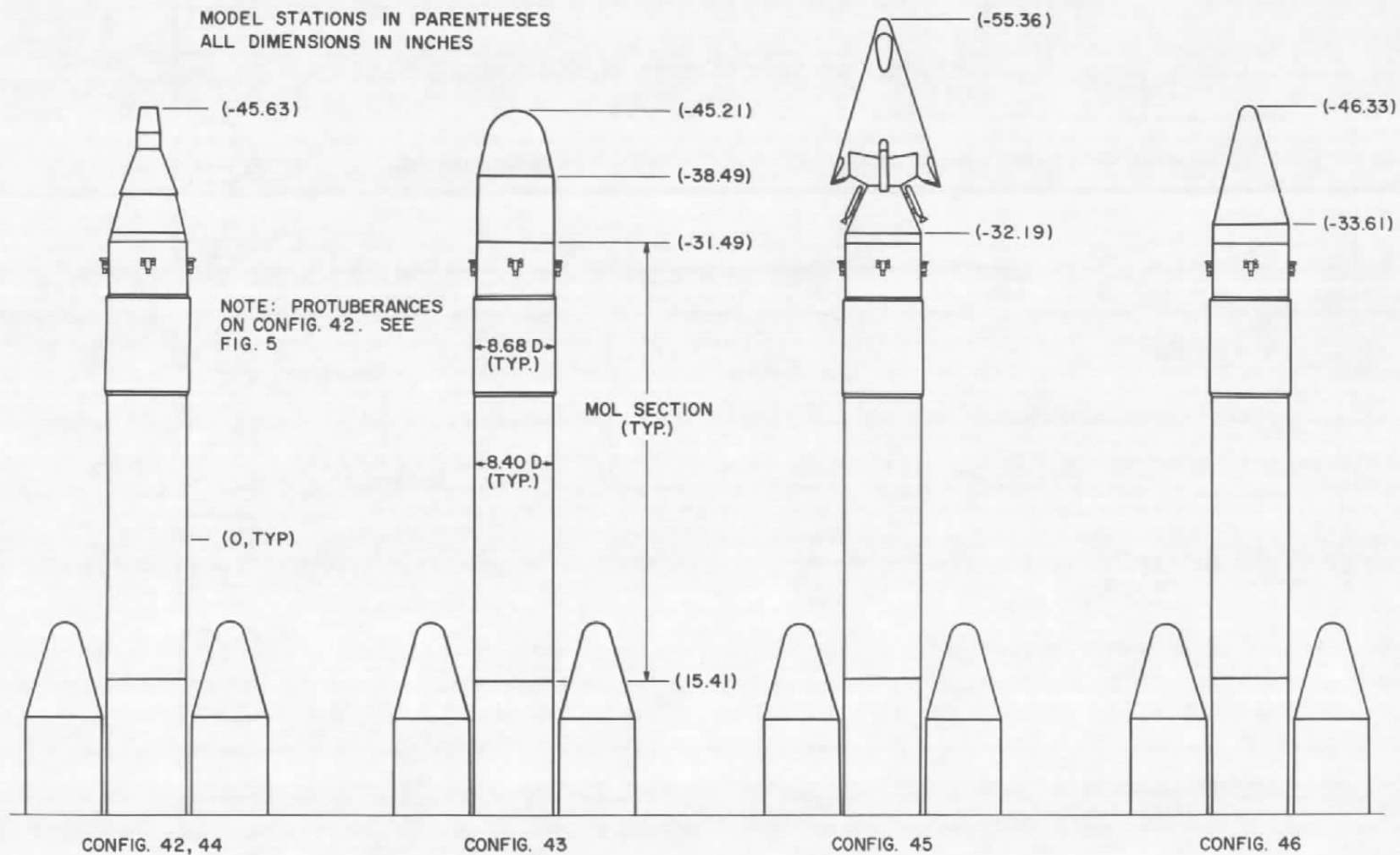


Fig. 4 Orientation of the Payloads on the Booster

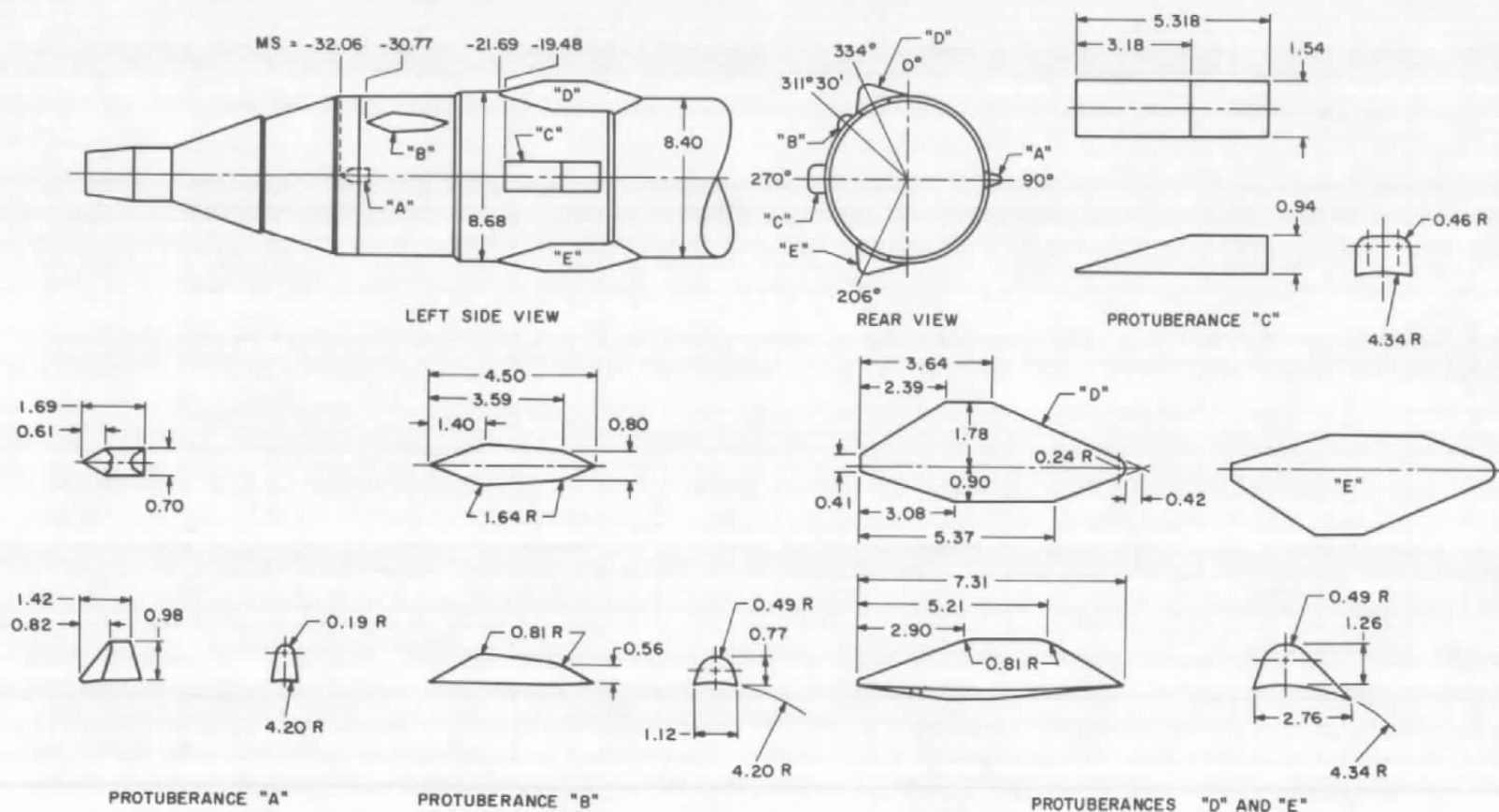
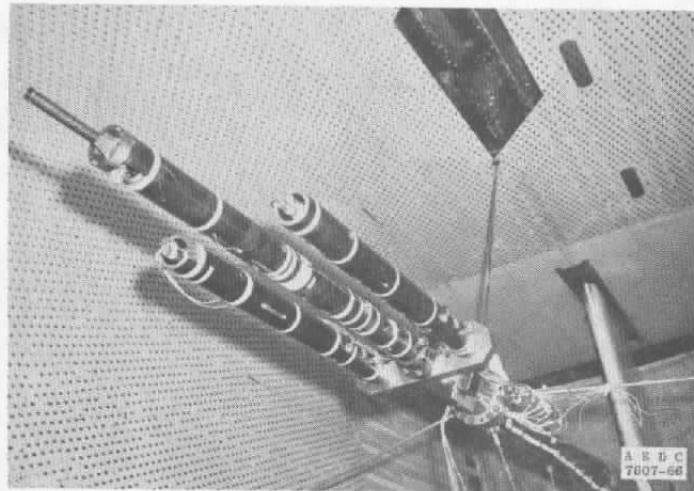
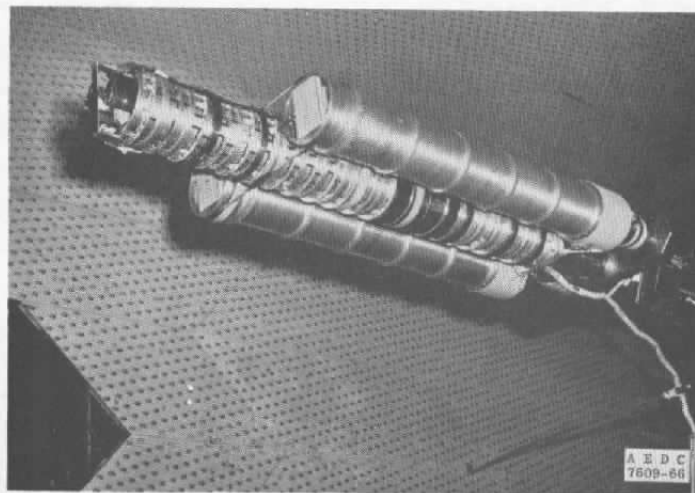


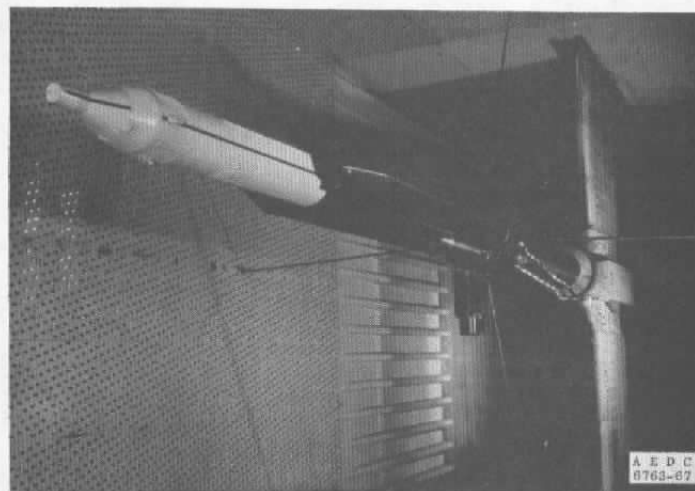
Fig. 5 Details of the Protuberances on the MOL, Configuration 42



a. Sting Support System

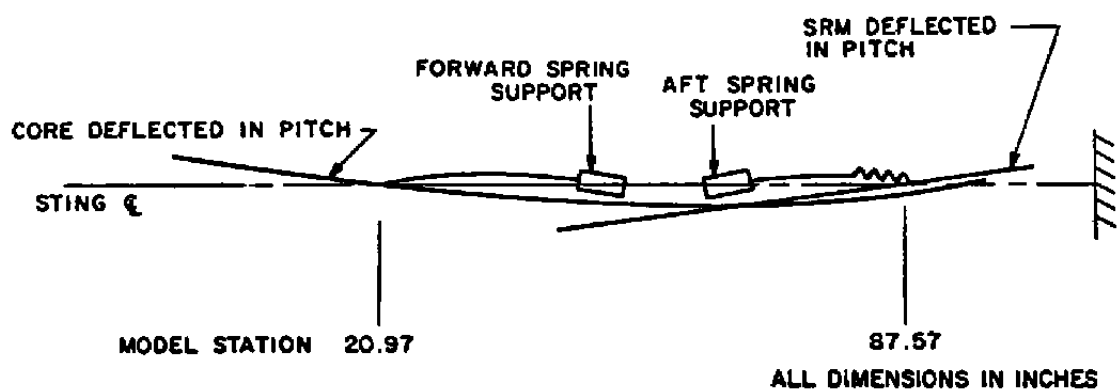


b. Elastic Structure with Concentrated Weights

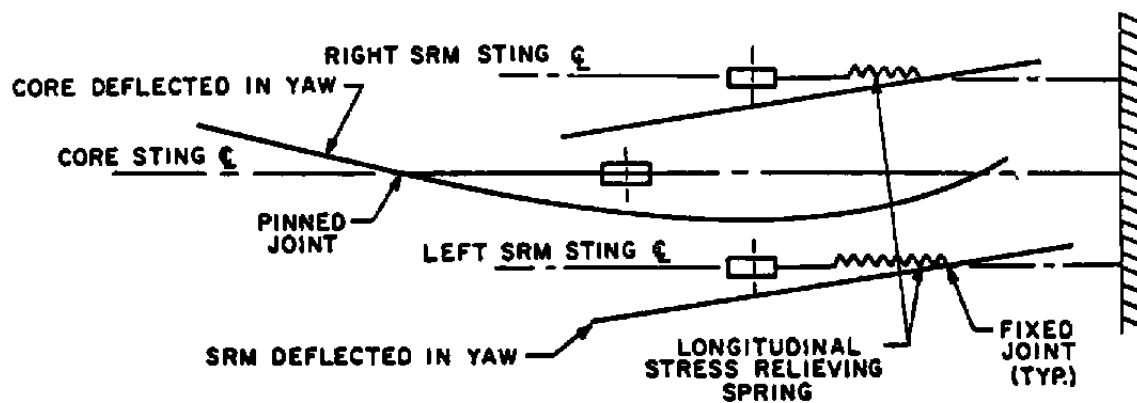


c. Assembled Model

Fig. 6 Photographs of the Model at Various Stages of Assembly



a. Side View



b. Top View

Fig. 7 Schematics of the Spring Support System

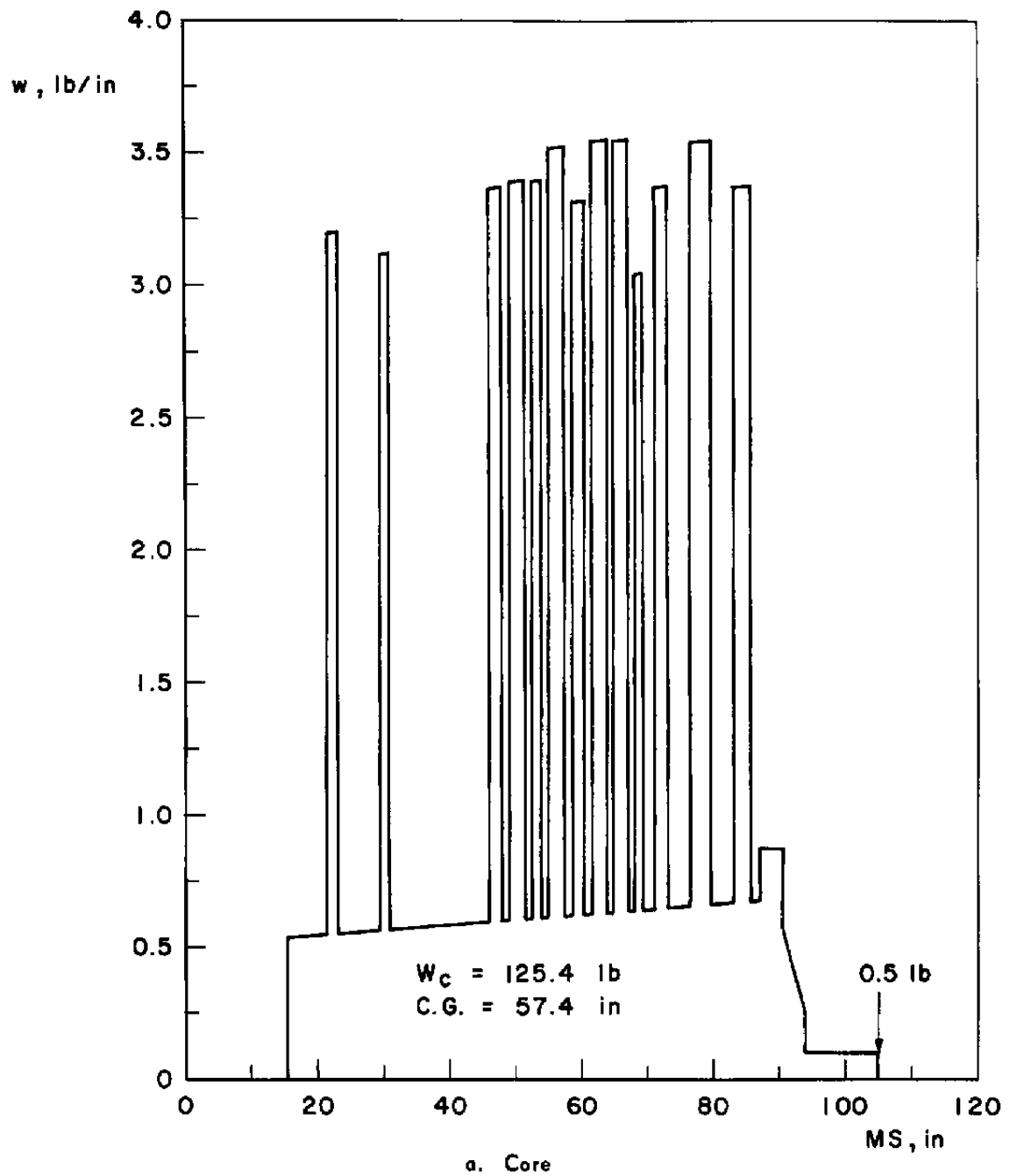


Fig. 8 Weight Distributions of the Model Components

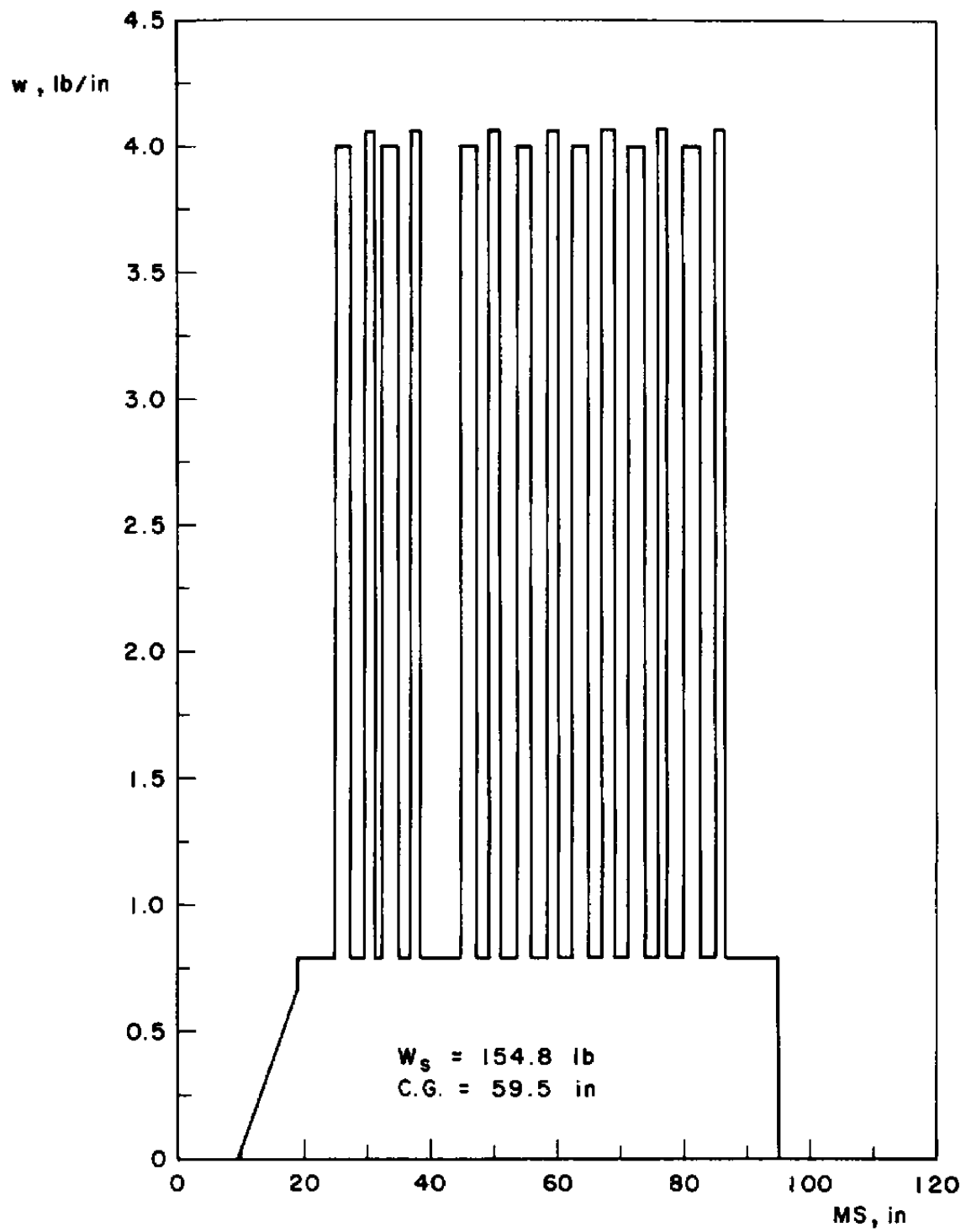
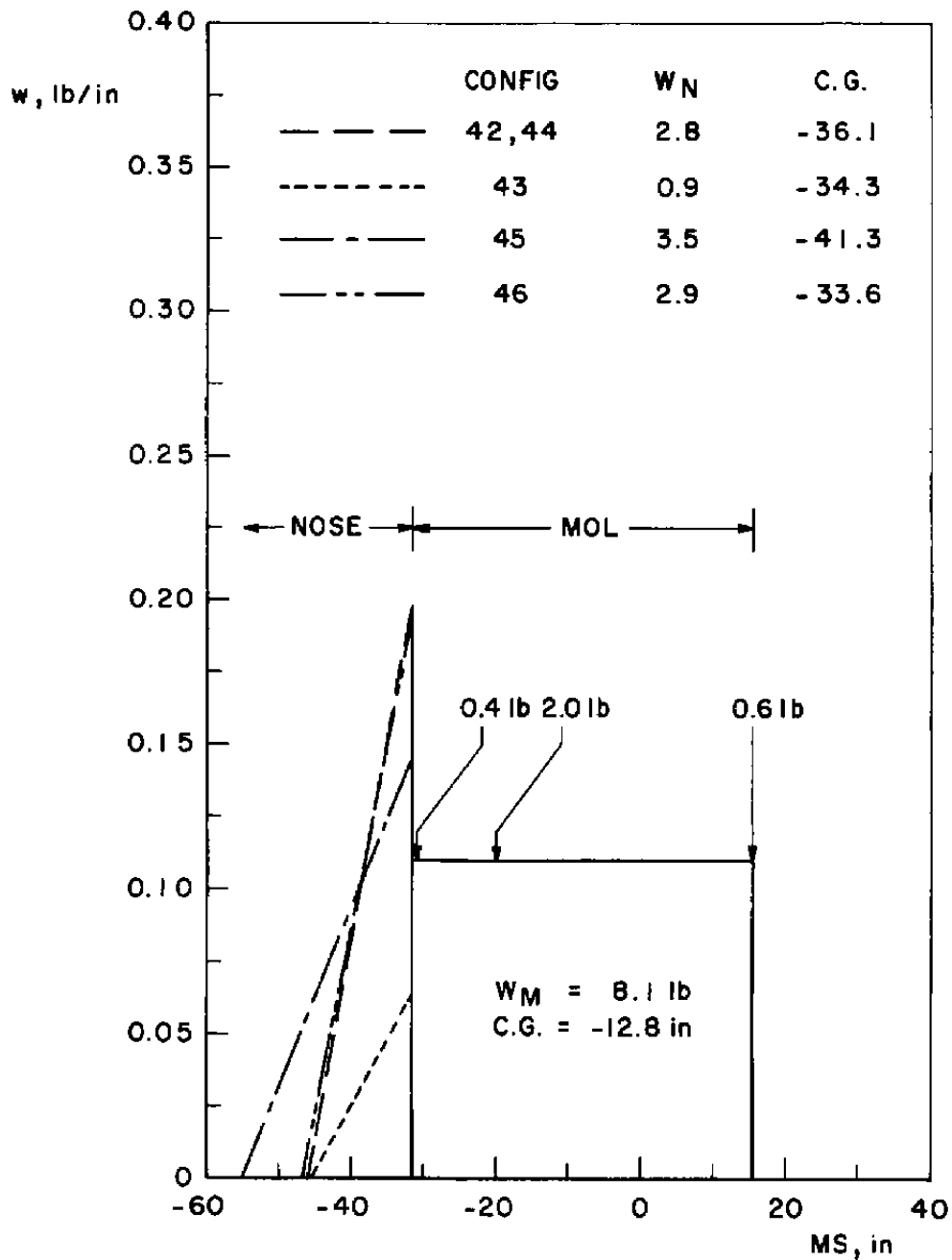
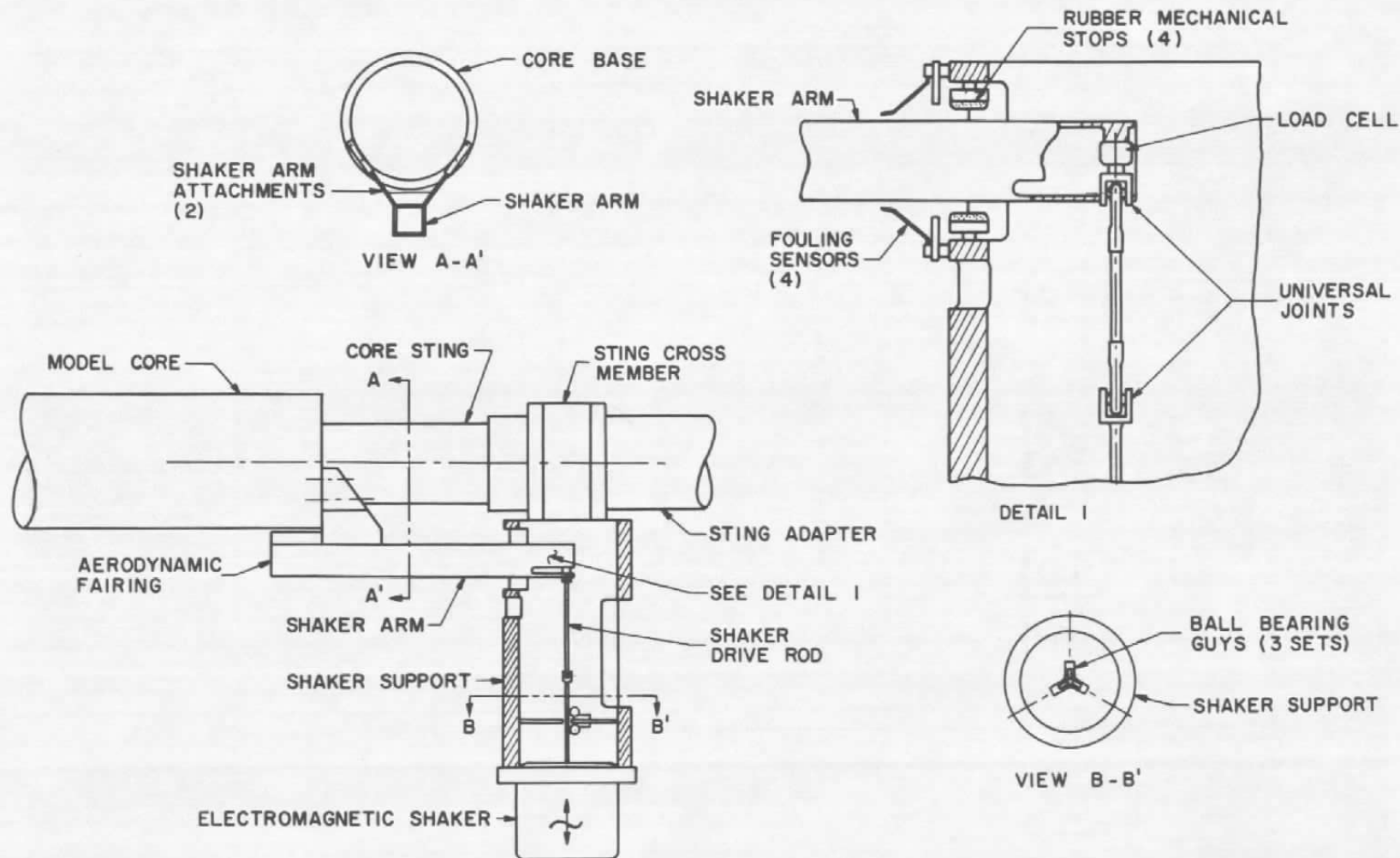


Fig. 8 Continued



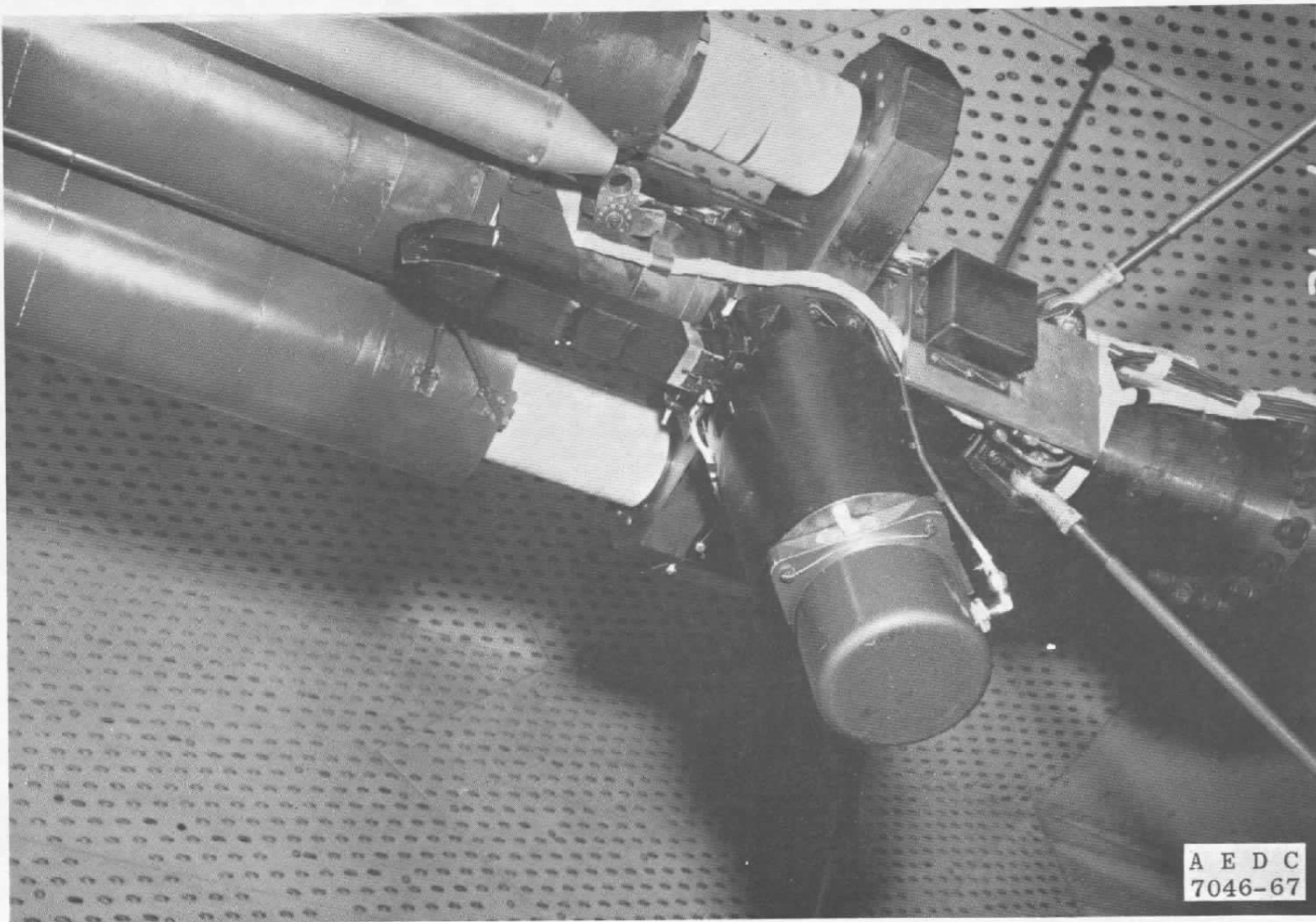
c. Payloads
Fig. 8 Concluded



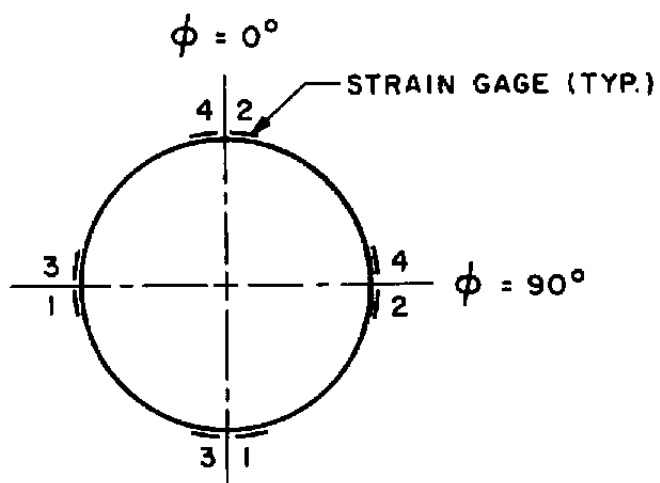
FORCED-OSCILLATION SHAKER SYSTEM

a. Installation Schematic

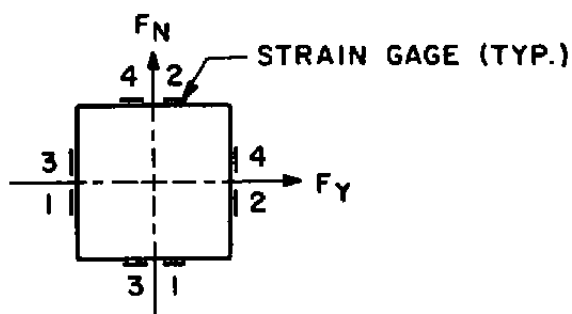
Fig. 9 Details of the Forced-Oscillation Shaker System



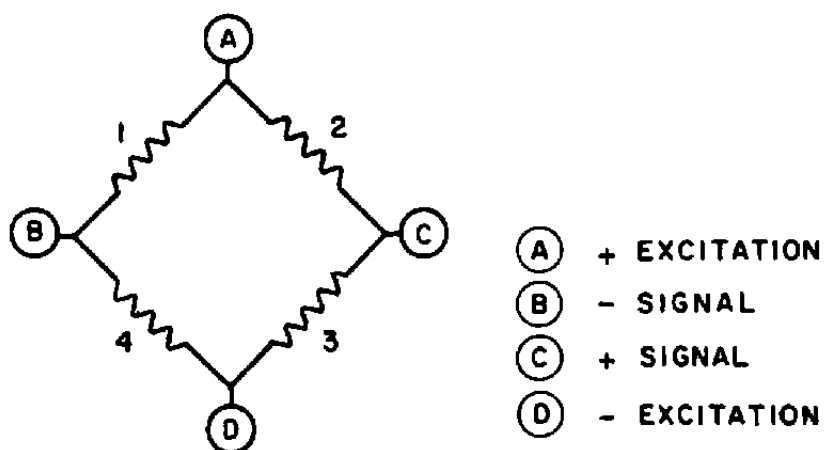
b. Installation Photograph
Fig. 9 Concluded



TYPICAL CORE CROSS SECTION



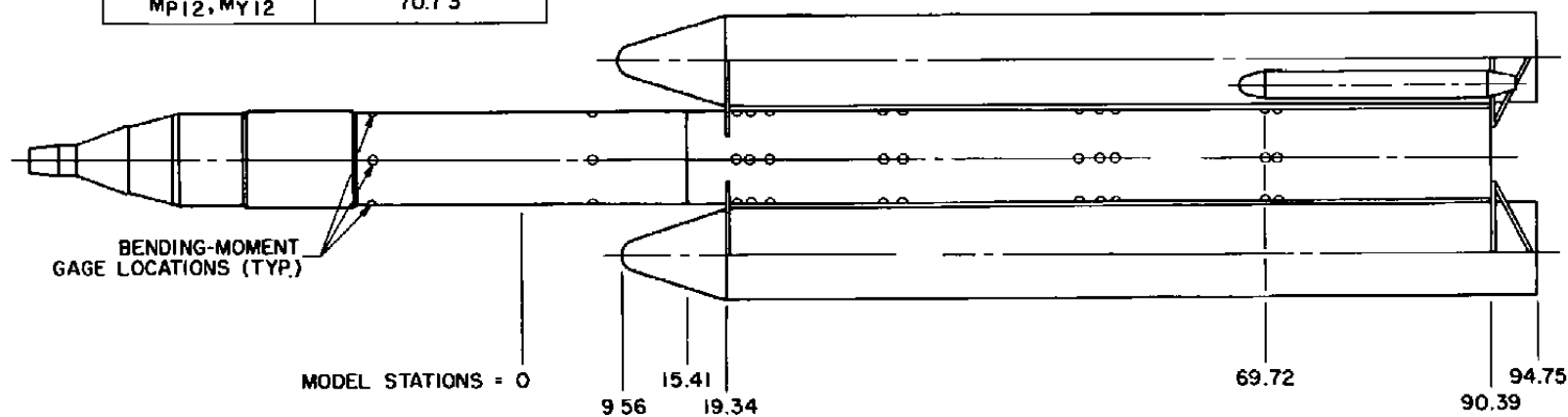
TYPICAL SUPPORT SPRING CROSS SECTION



TYPICAL SENSOR

Fig. 10 Details of the Bending-Moment and Support Spring Force Sensors

BENDING-MOMENT SENSOR LOCATIONS	
SENSOR	MODEL STATION
Mp1 , My1	- 13.84
Mp2 , My2	6.86
Mp3 , My3	20.16
Mp4 , My4	21.41
Mp5 , My5	23.16
Mp6 , My6	33.73
Mp7 , My7	35.48
Mp8 , My8	51.98
Mp9 , My9	53.98
Mp10, My10	55.36
Mp11, My11	69.41
Mp12, My12	70.73



ALL DIMENSIONS IN INCHES

Fig. 11 Axial Locations of the Bending-Moment Sensors

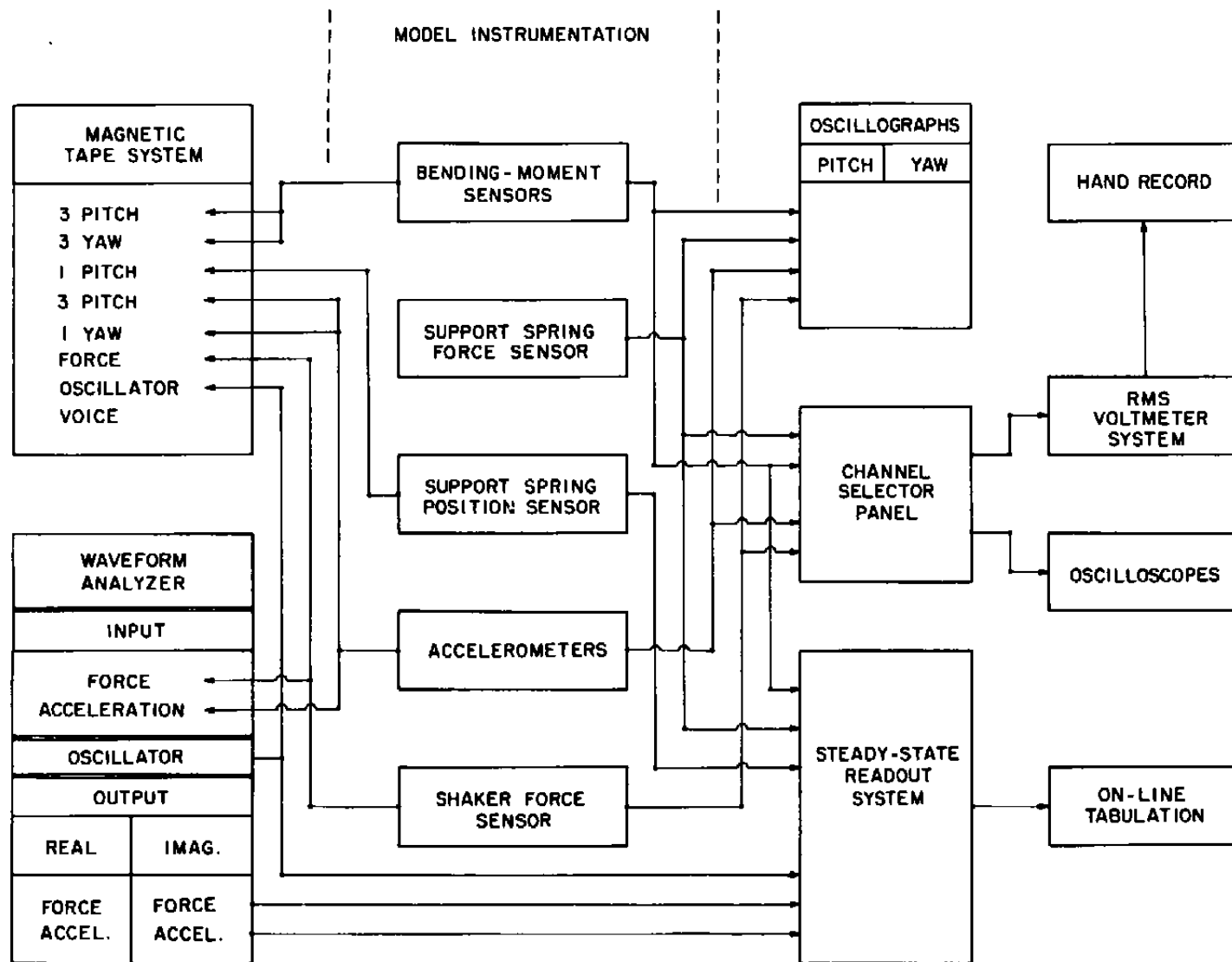
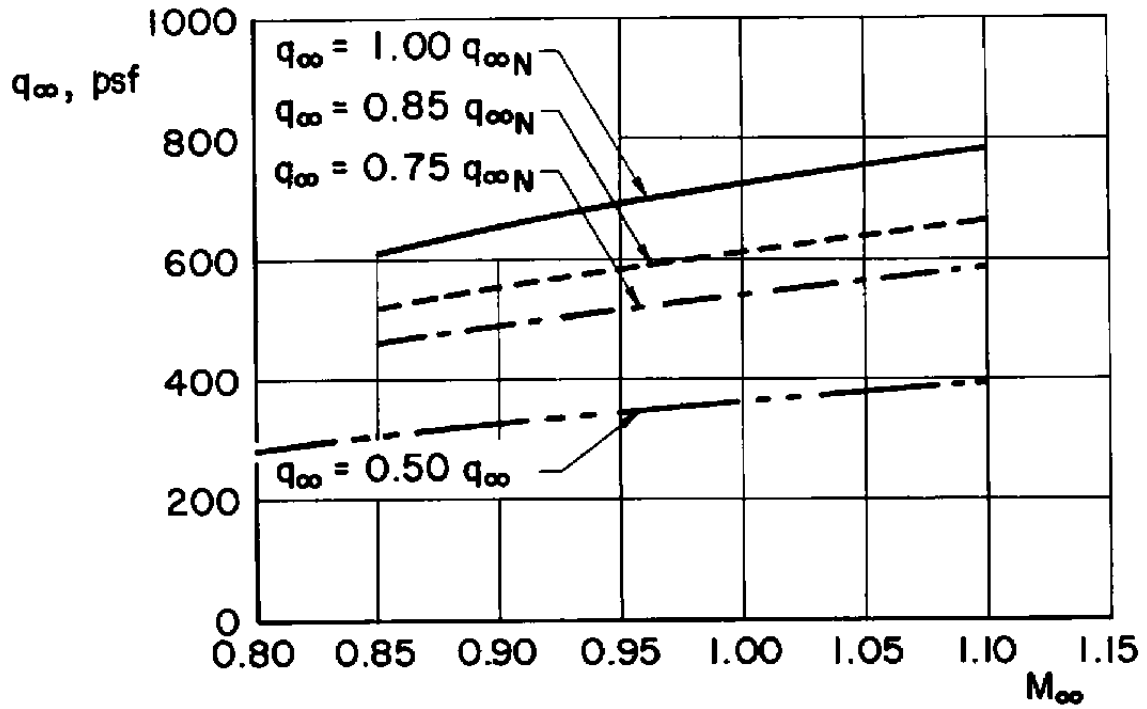
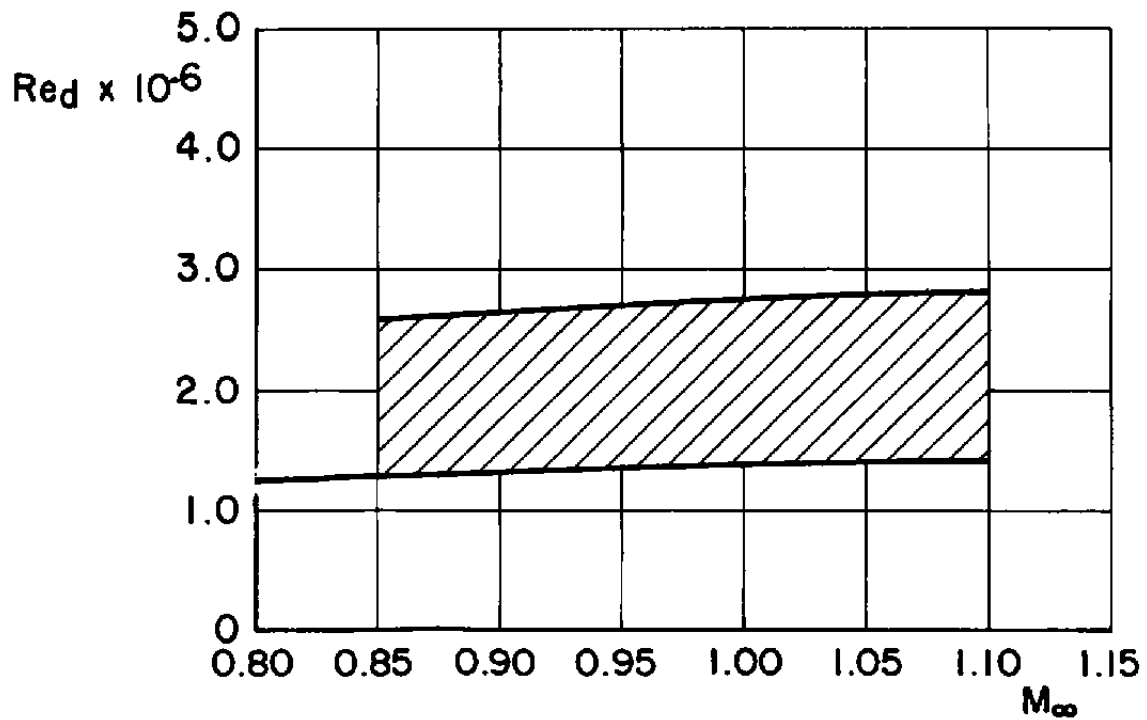


Fig. 12 Data Acquisition System



a. Dynamic Pressure



b. Reynolds Number

Fig. 13 Variation of Dynamic Pressure and Reynolds Number with Mach Number

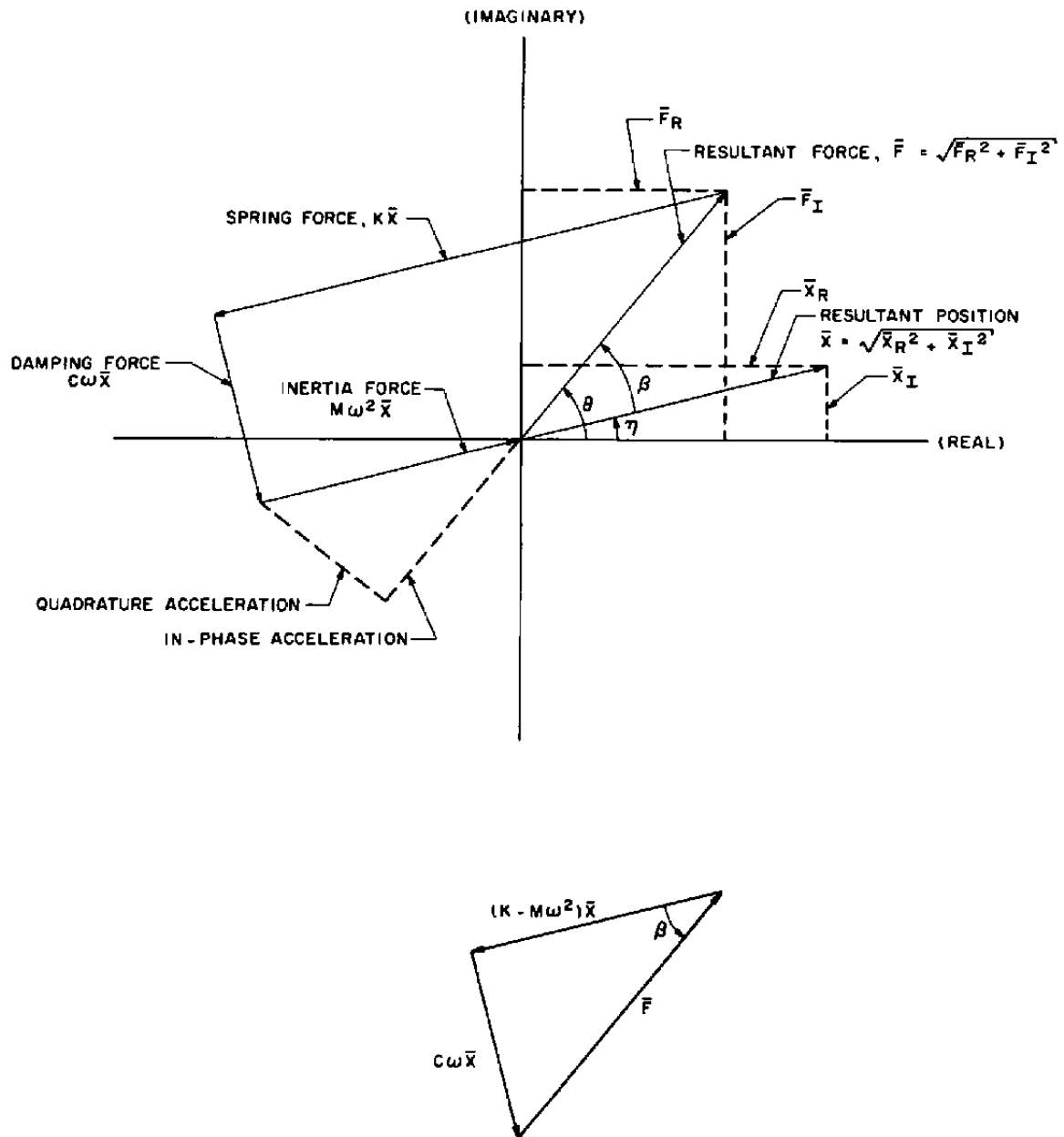


Fig. 14 Vector Representation of a Single-Degree-of-Freedom, Forced-Oscillation System with Viscous Damping

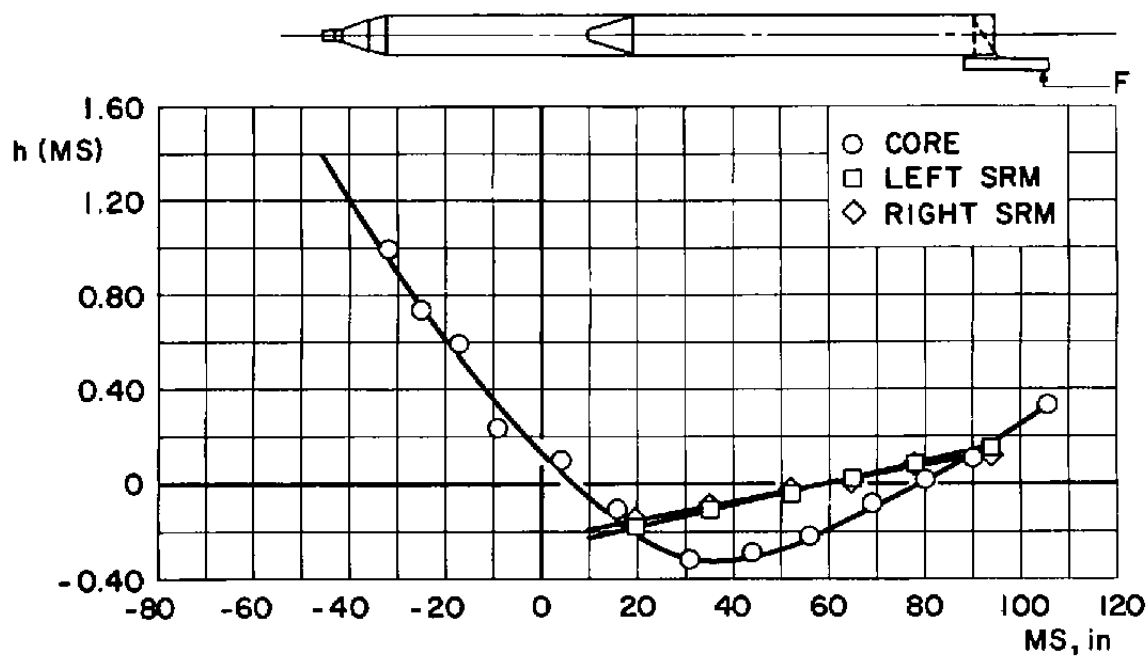
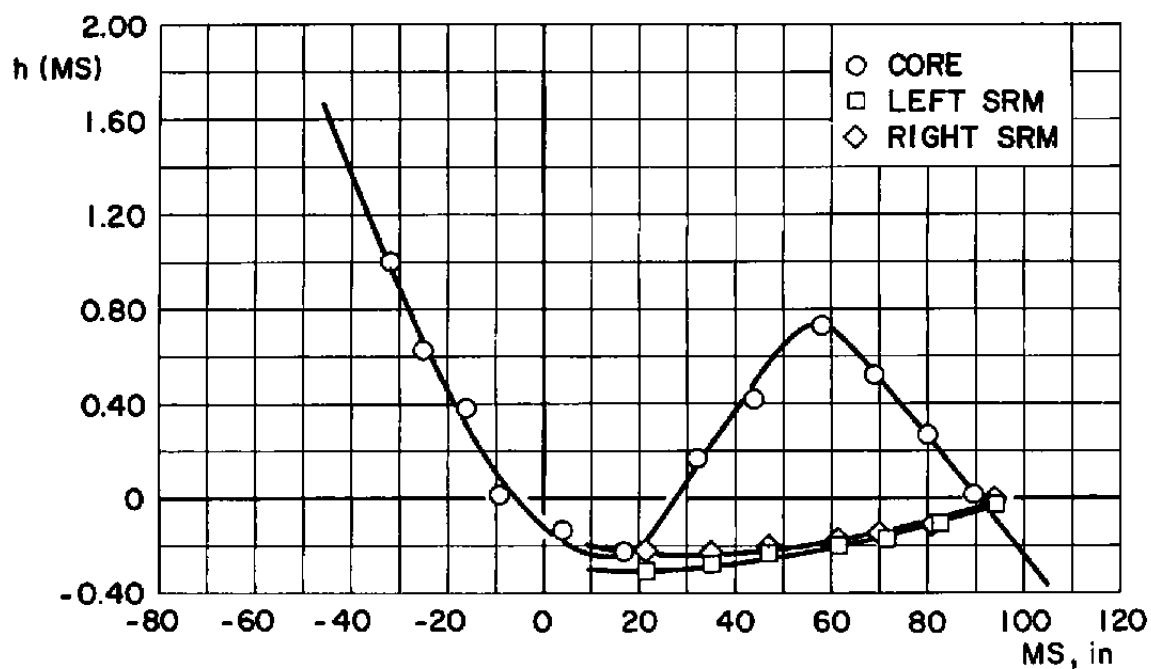
a. First Pitch Bending Mode, $f_o = 17.87$ b. Second Pitch Bending Mode, $f_o = 31.87$

Fig. 15 Longitudinal Variation of the Normalized Modal Deflection for Configuration 42

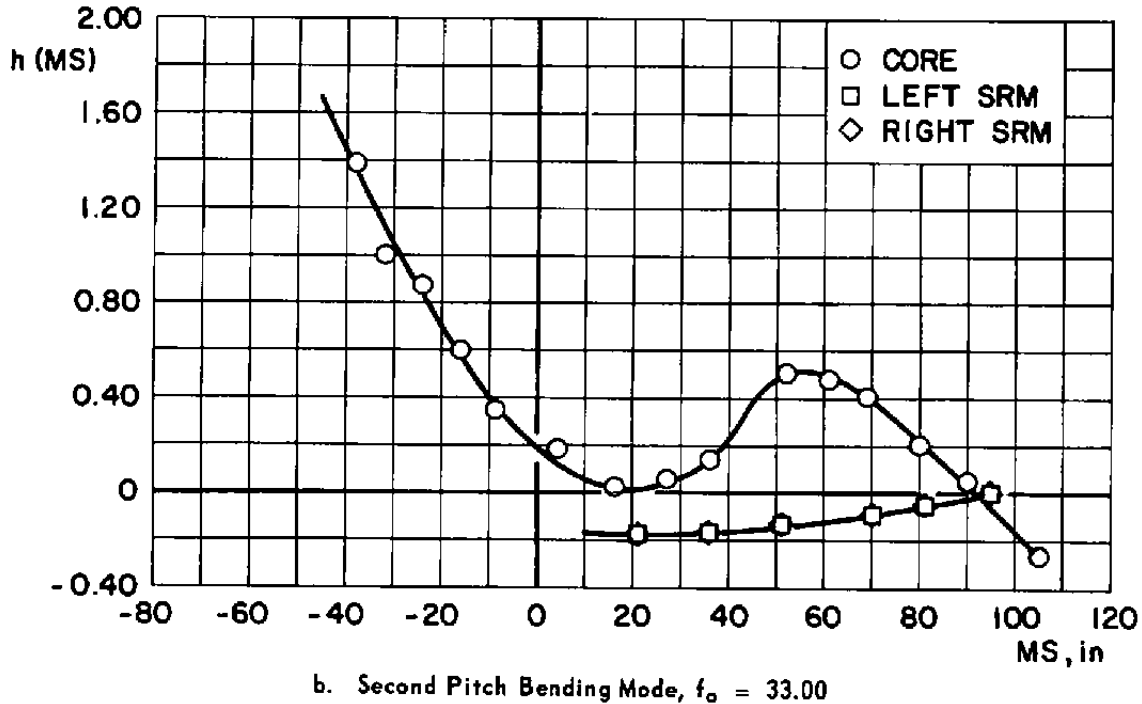
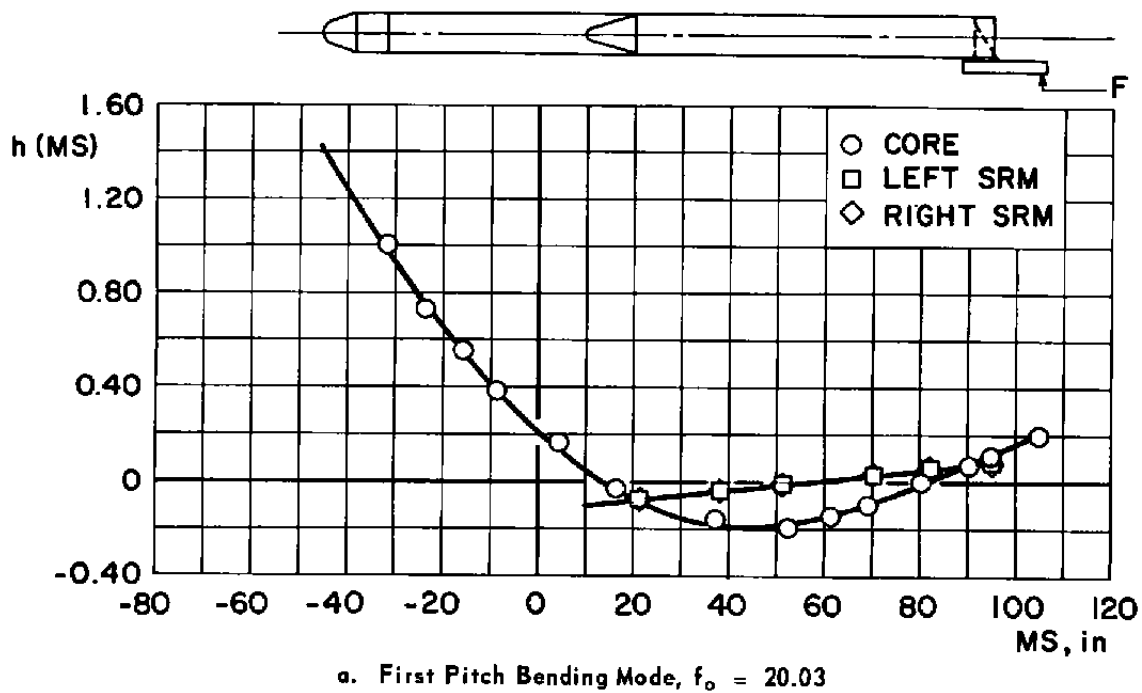


Fig. 16 Longitudinal Variation of the Normalized Modal Deflection for Configuration 43

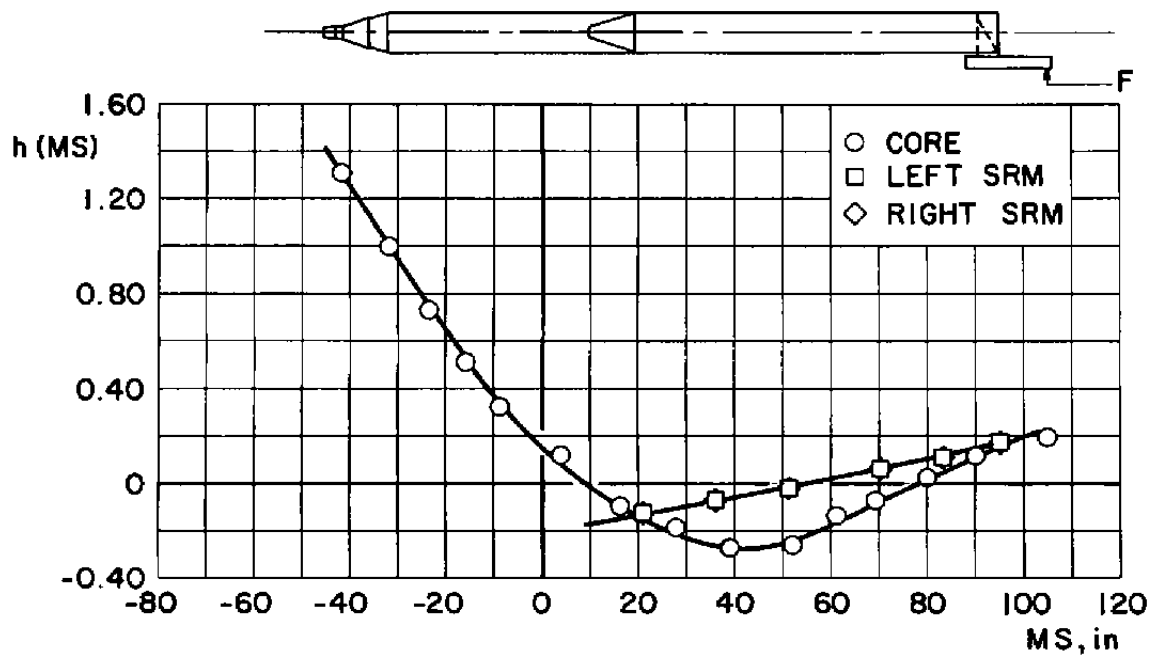
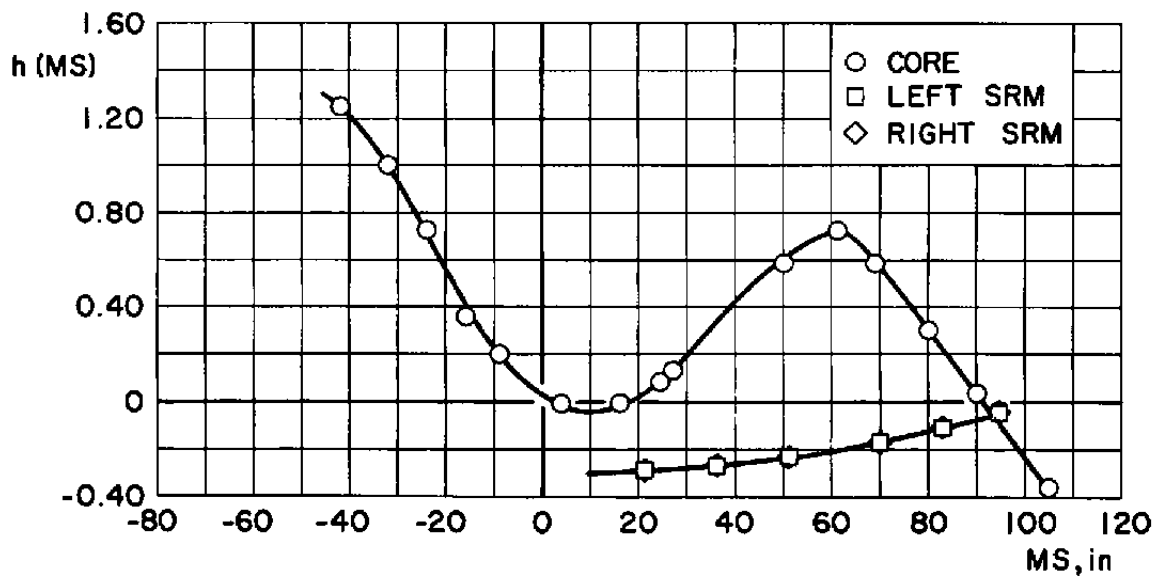
a. First Pitch Bending Mode, $f_o = 17.77$ b. Second Pitch Bending Mode, $f_o = 31.28$

Fig. 17 Longitudinal Variation of the Normalized Modal Deflection for Configuration 44

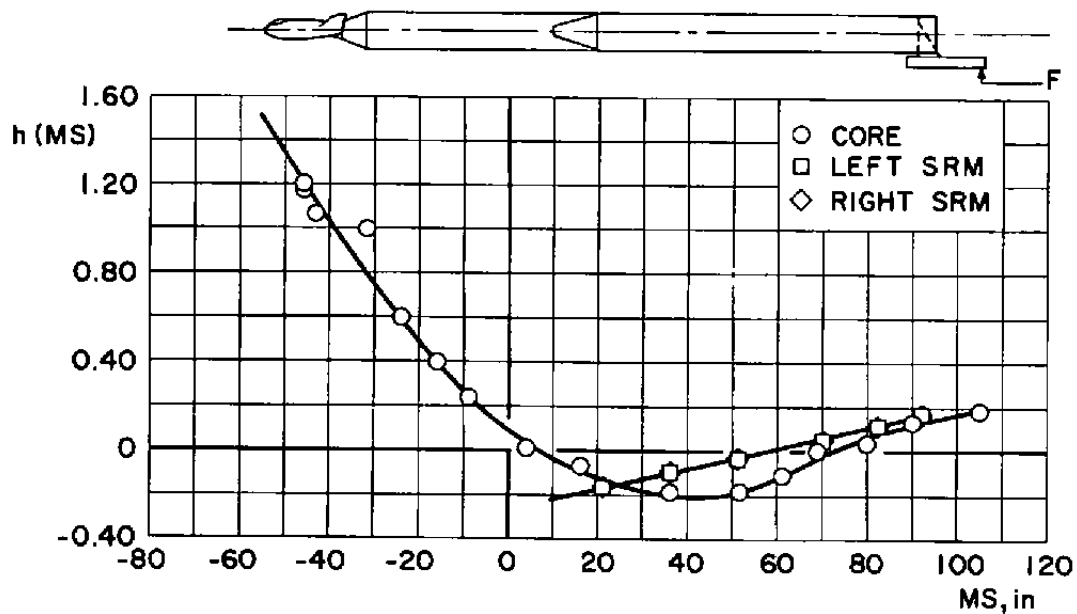
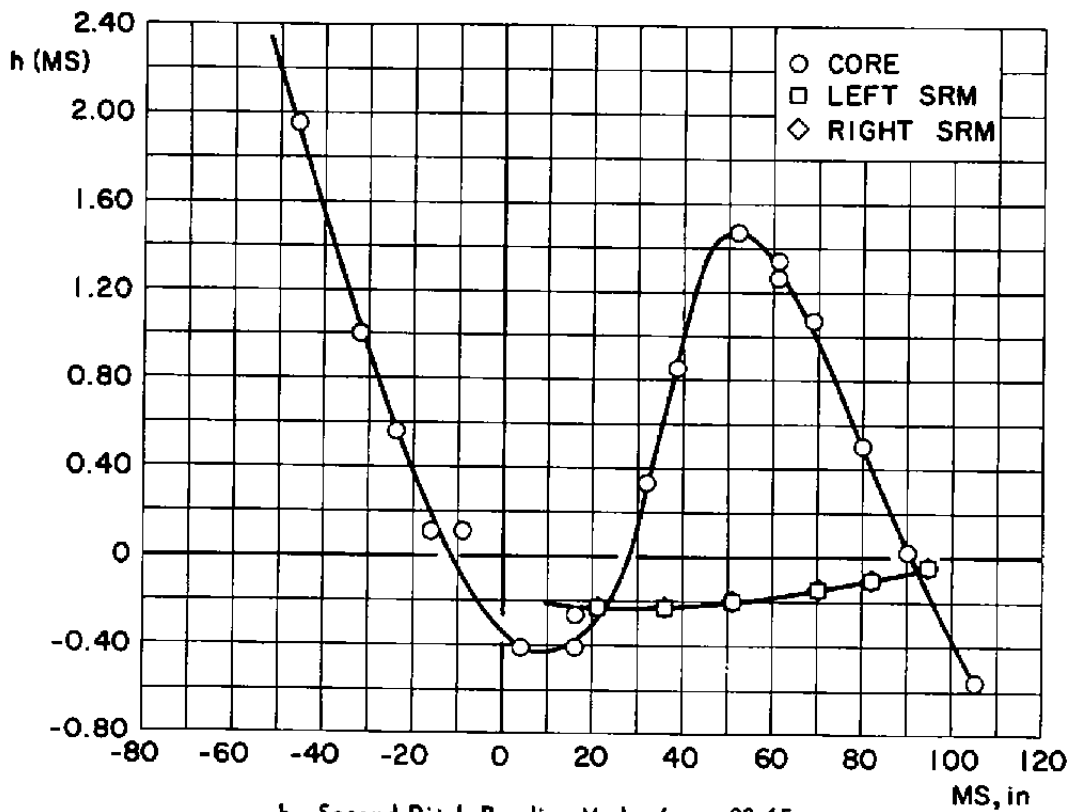
a. First Pitch Bending Mode, $f_o = 16.43$ b. Second Pitch Bending Mode, $f_o = 30.65$

Fig. 18 Longitudinal Variation of the Normalized Modal Deflection for Configuration 45

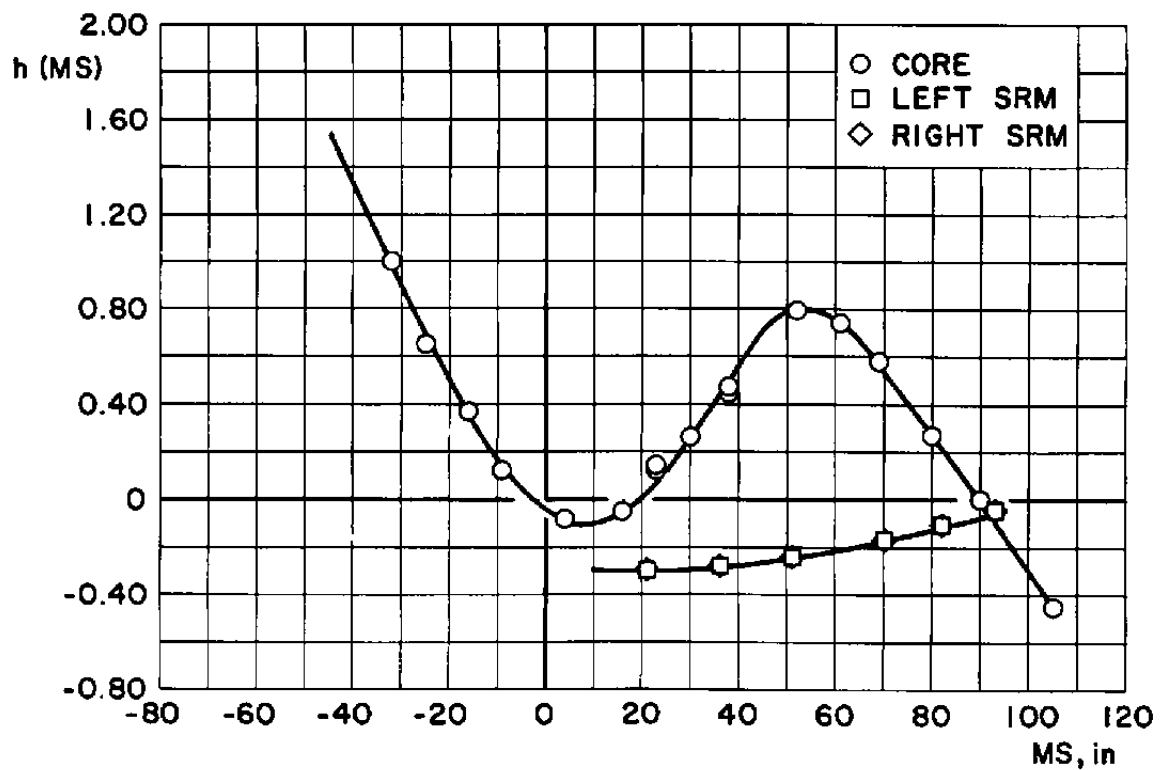
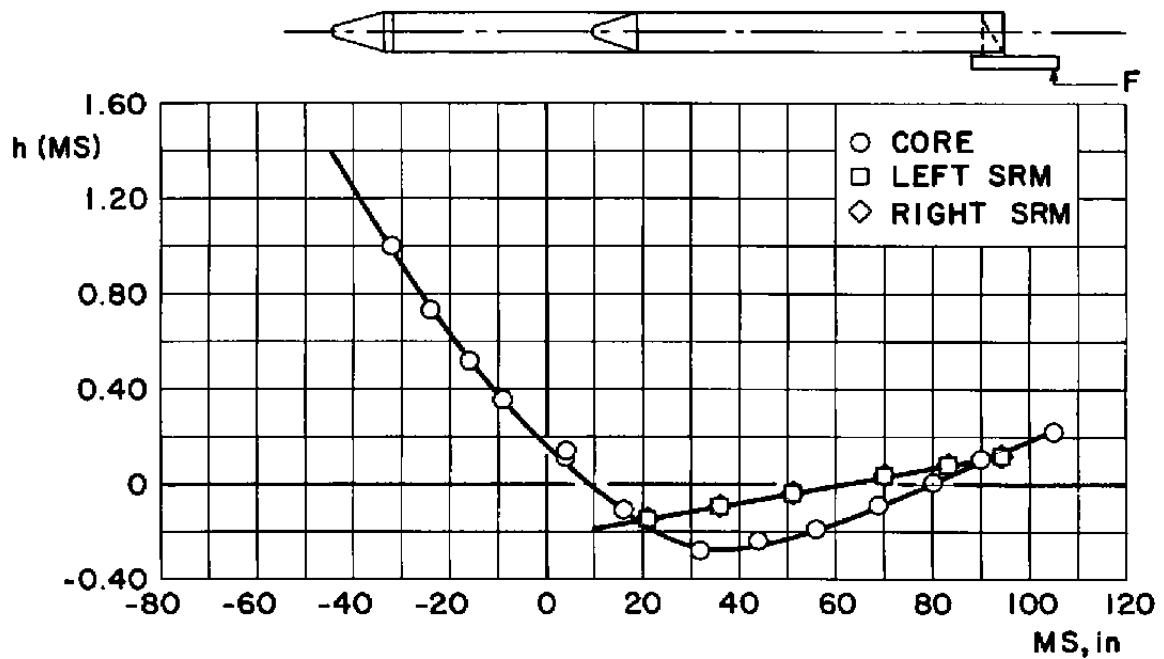
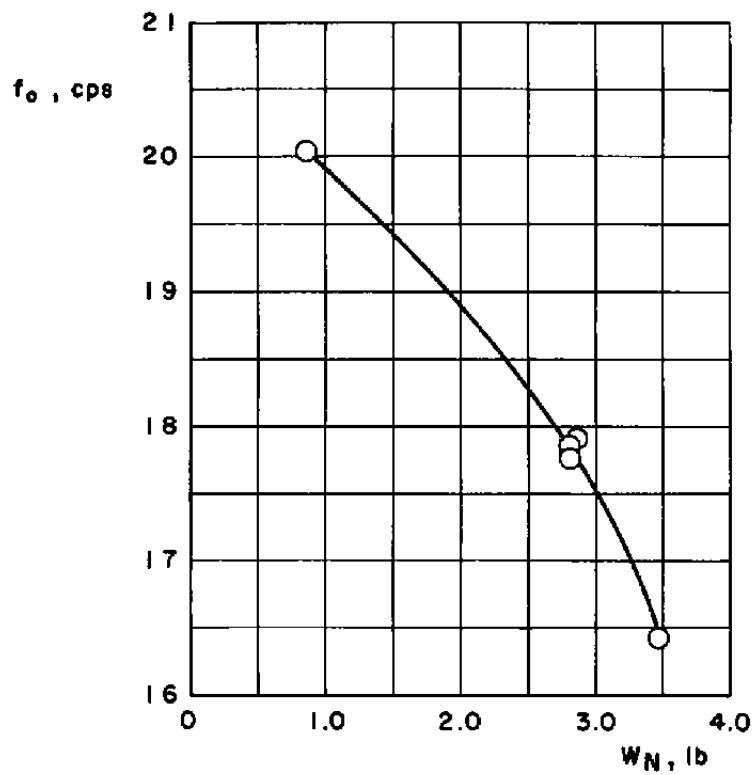
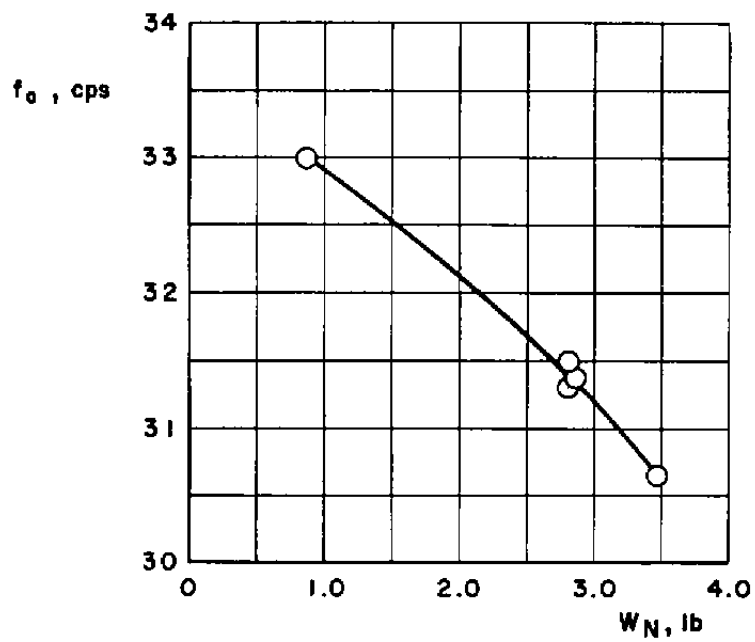


Fig. 19 Longitudinal Variation of the Normalized Modal Deflection for Configuration 46

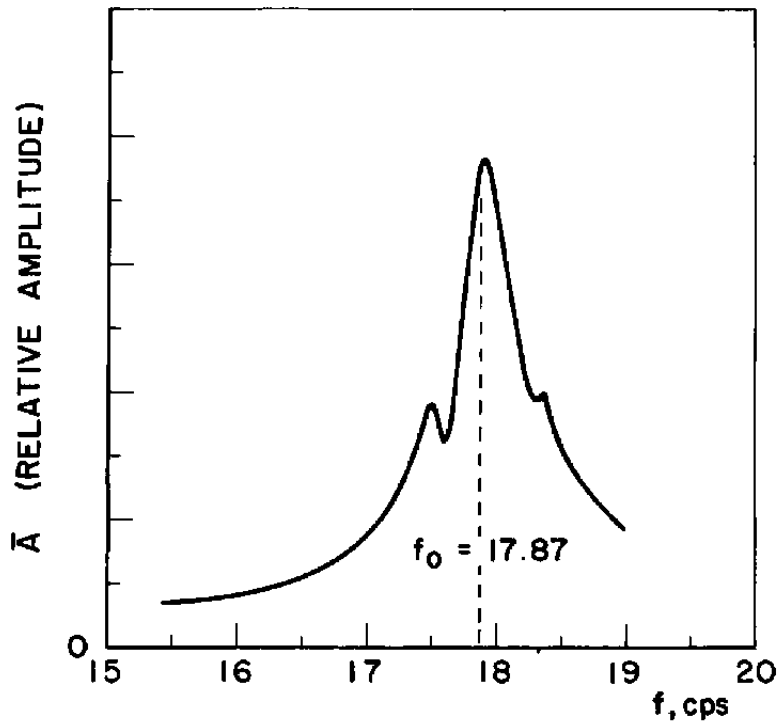


a. First Pitch Bending Mode

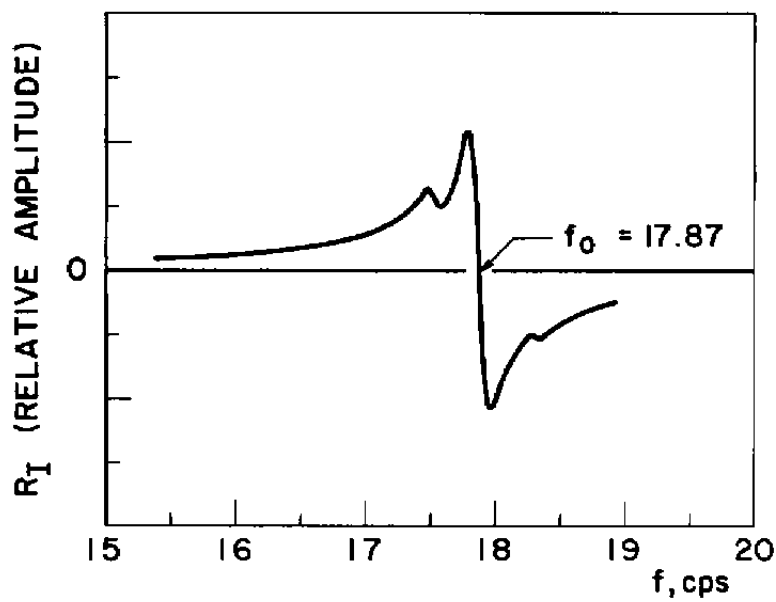


b. Second Pitch Bending Mode

Fig. 20 Effects of Nose Weight on Resonance Frequency

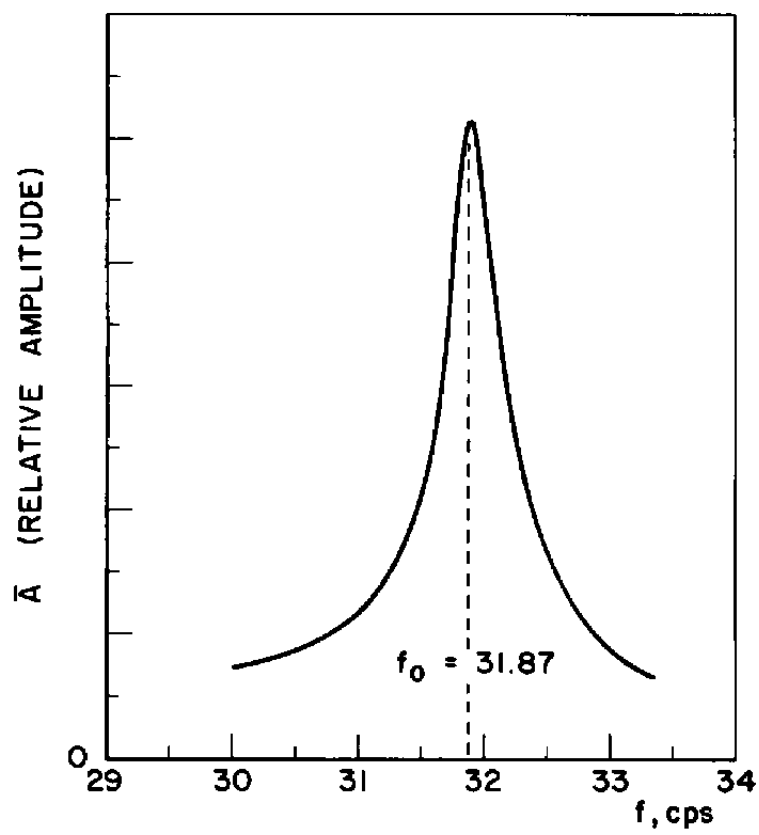


a. Total Acceleration

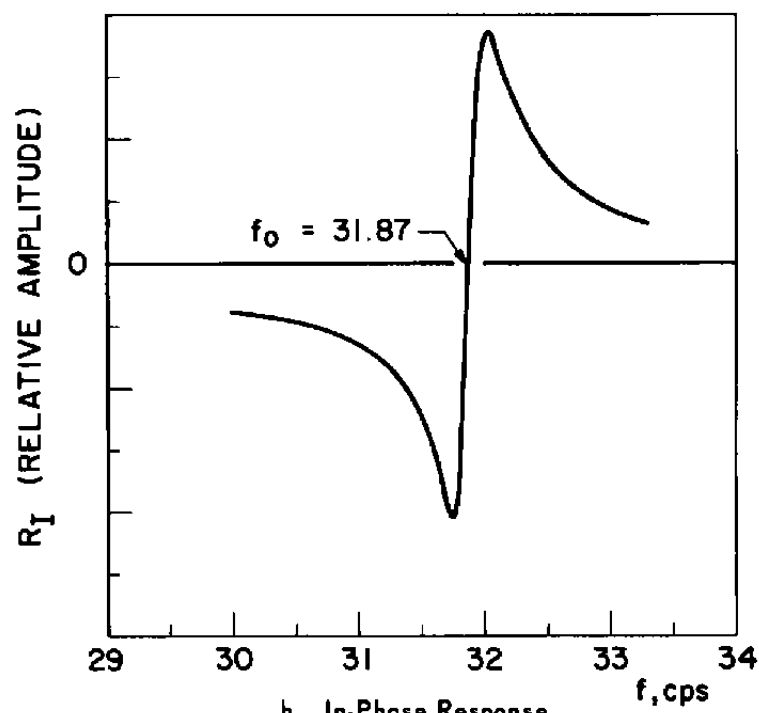


b. In-Phase Response

Fig. 21 Variation of the Total Acceleration and In-Phase Response with Frequency, Configuration 42, First Mode

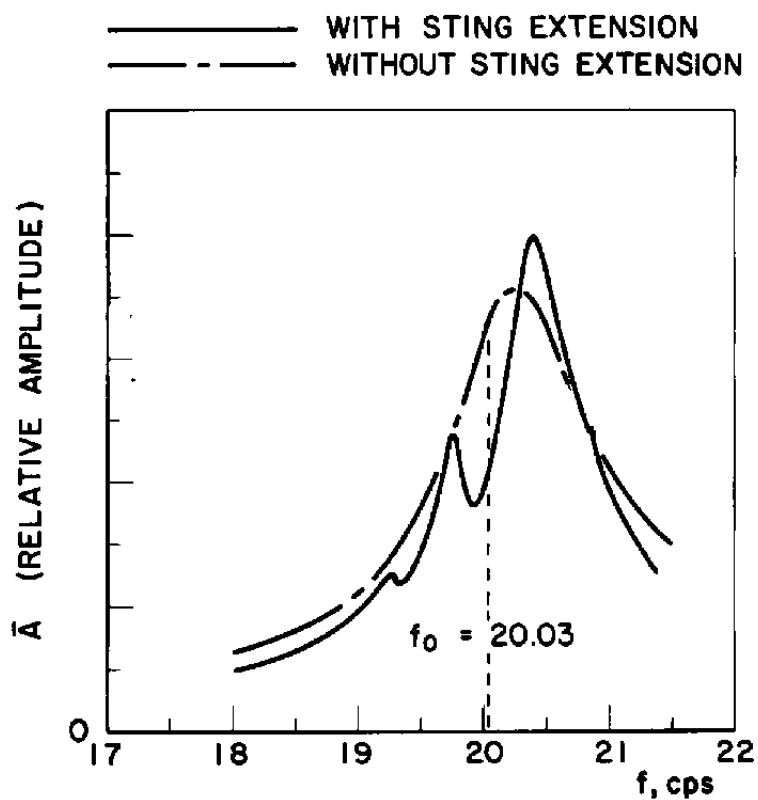


a. Total Acceleration

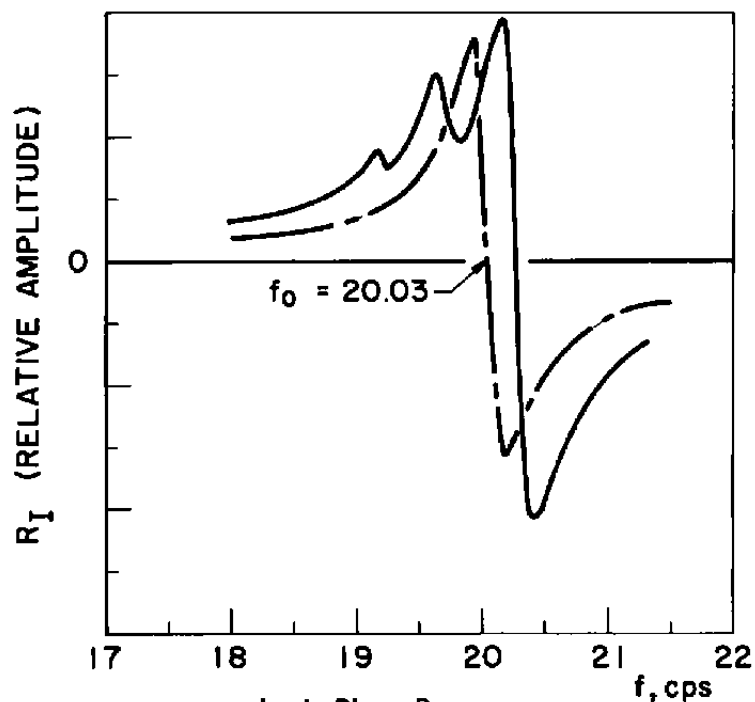


b. In-Phase Response

Fig. 22 Variation of the Total Acceleration and In-Phase Response with Frequency, Configuration 42, Second Mode

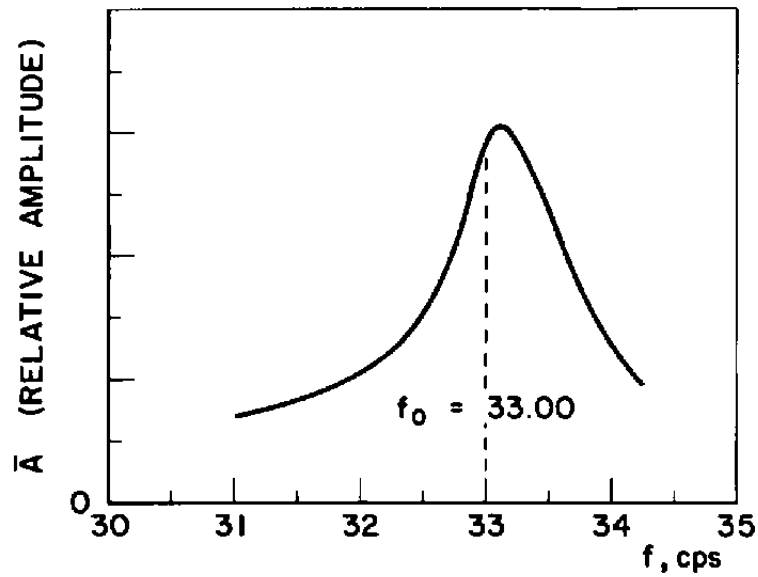


a. Total Acceleration

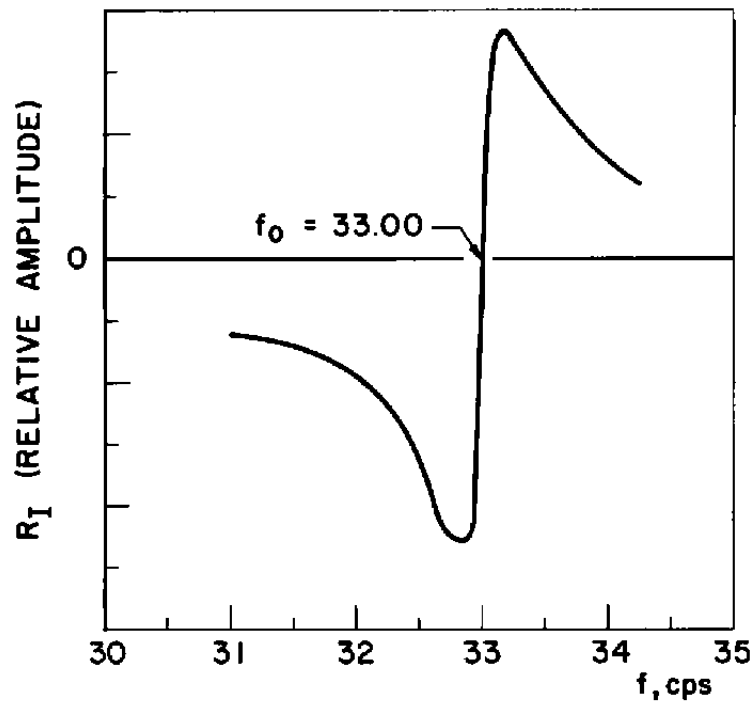


b. In-Phase Response

Fig. 23 Variation of the Total Acceleration and In-Phase Response with Frequency, Configuration 43, First Mode

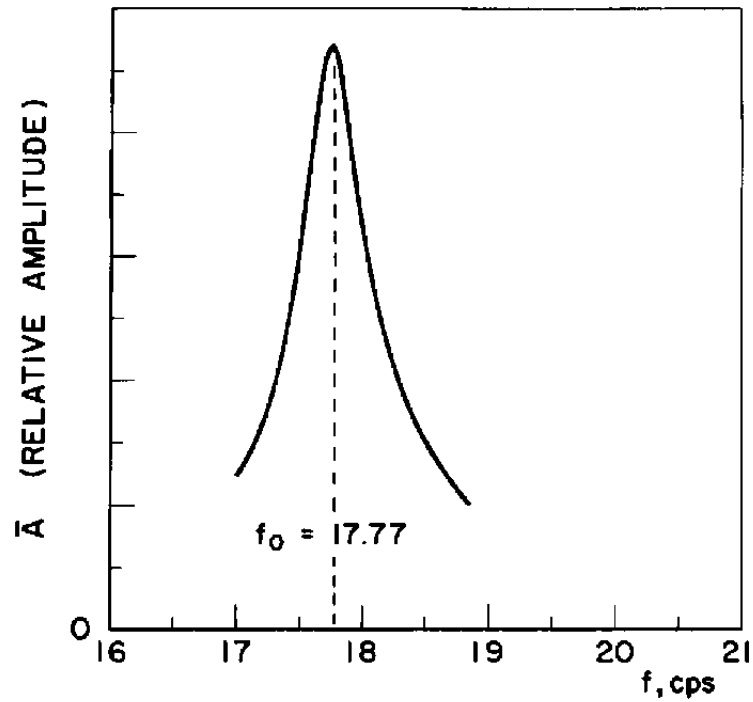


a. Total Acceleration

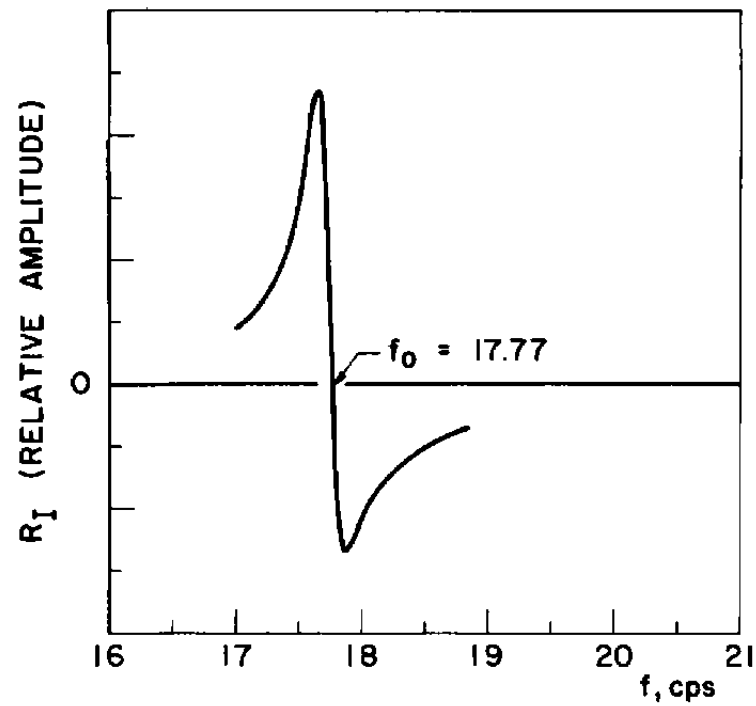


b. In-Phase Response

Fig. 24 Variation of the Total Acceleration and In-Phase Response with Frequency, Configuration 43, Second Mode

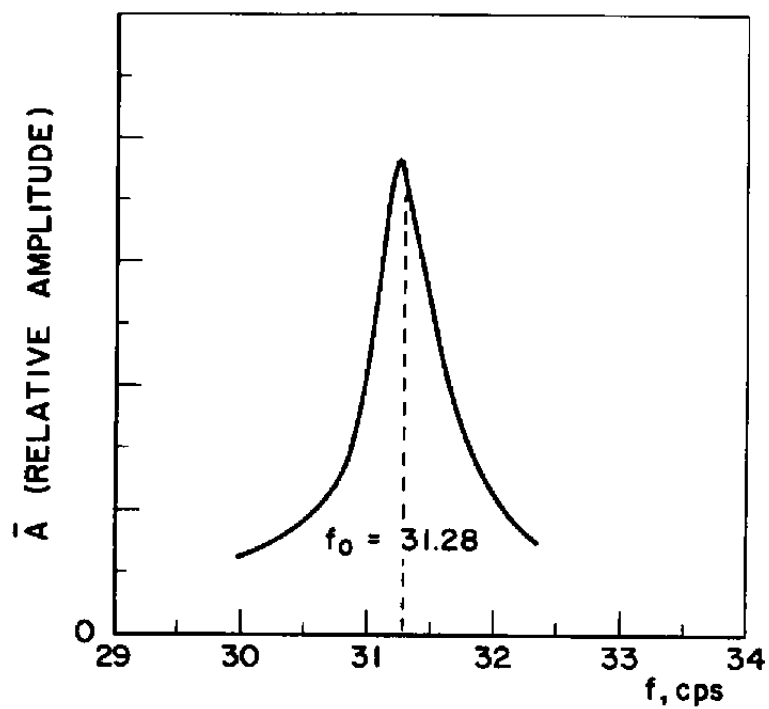


a. Total Acceleration

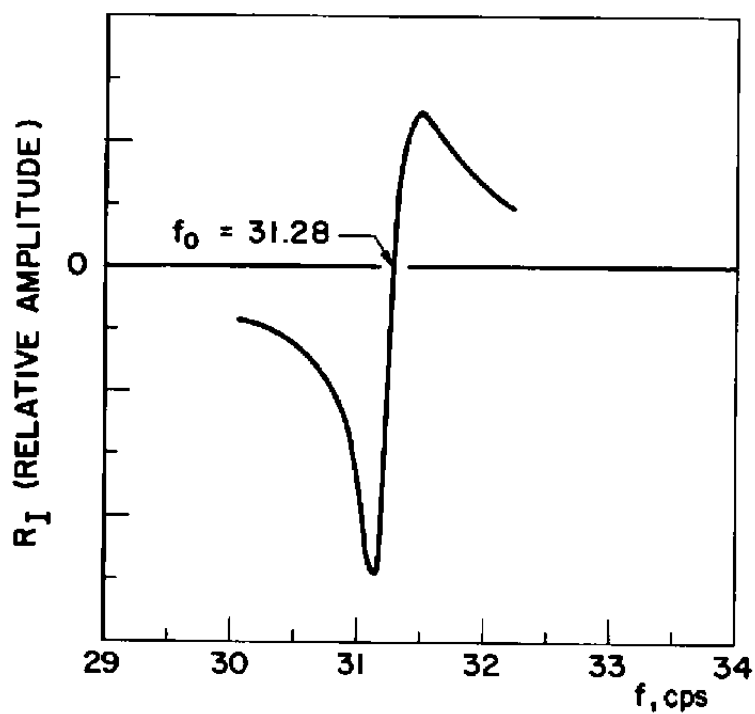


b. In-Phase Response

Fig. 25 Variation of the Total Acceleration and In-Phase Response with Frequency, Configuration 44, First Mode

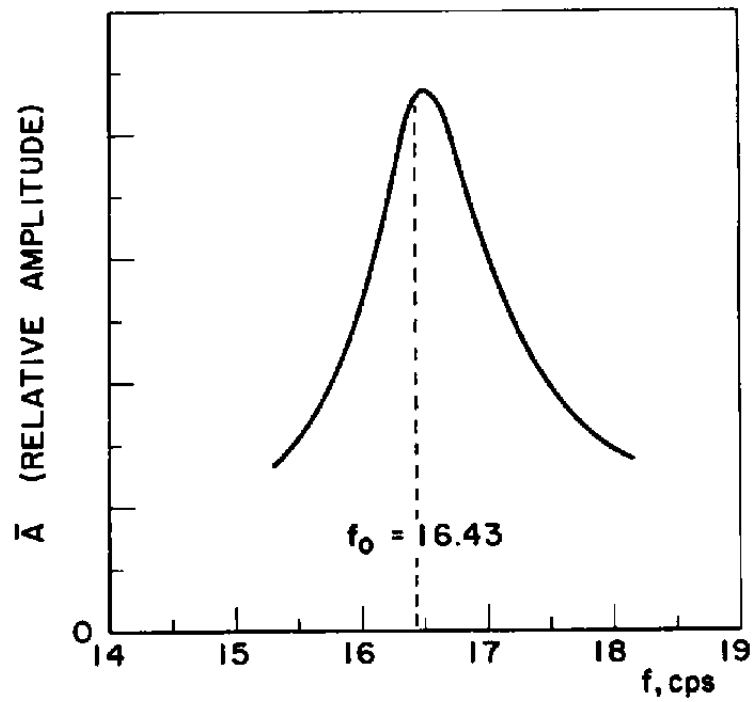


a. Total Acceleration

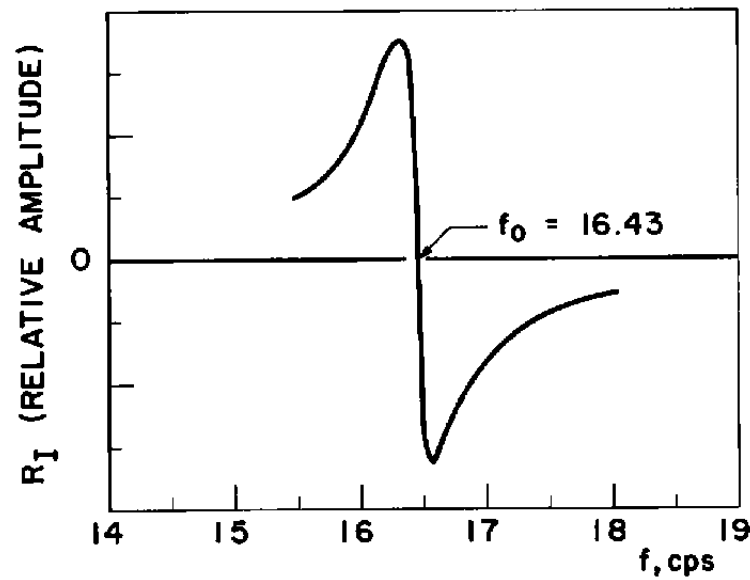


b. In-Phase Response

Fig. 26 Variation of the Total Acceleration and In-Phase Response with Frequency, Configuration 44, Second Mode

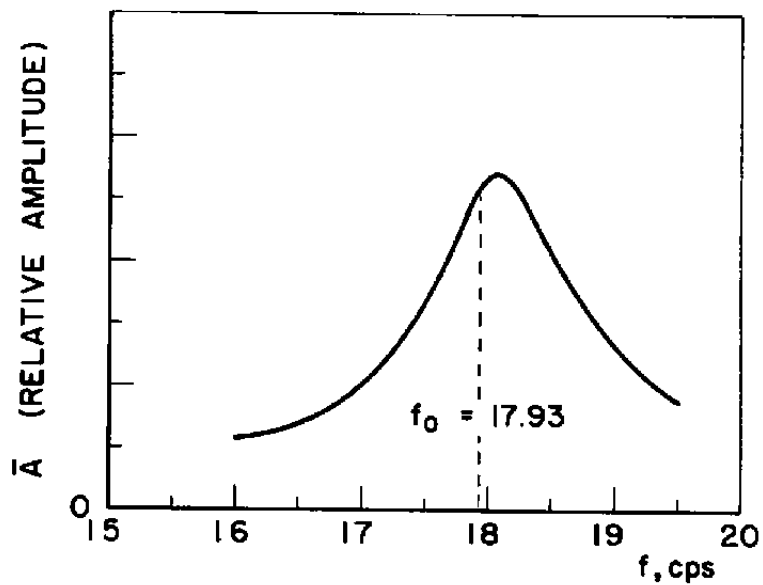


a. Total Acceleration

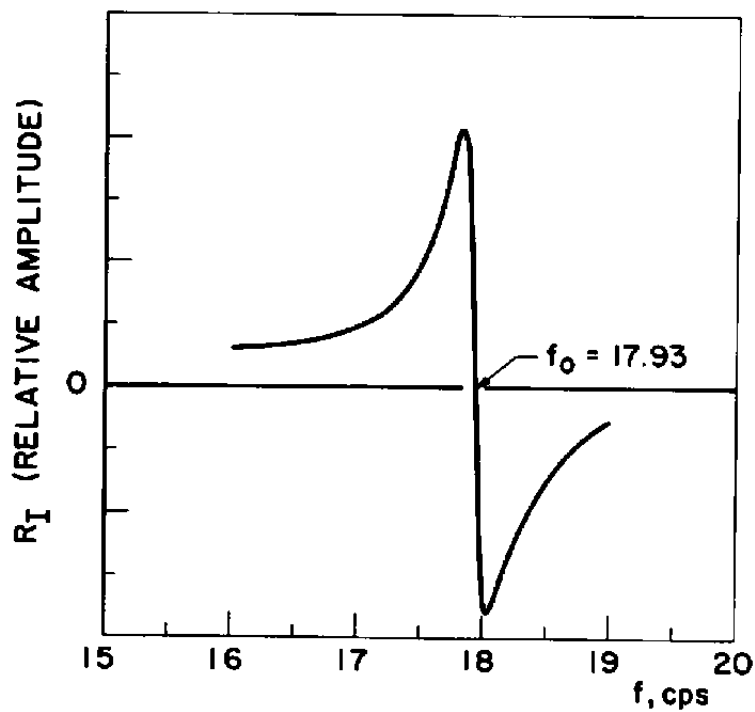


b. In-Phase Response

Fig. 27 Variation of the Total Acceleration and In-Phase Response with Frequency, Configuration 45, First Mode

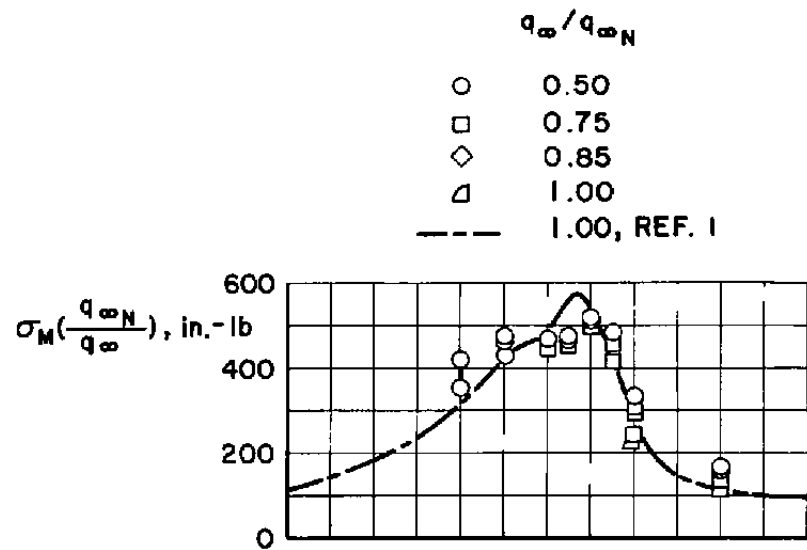


a. Total Acceleration

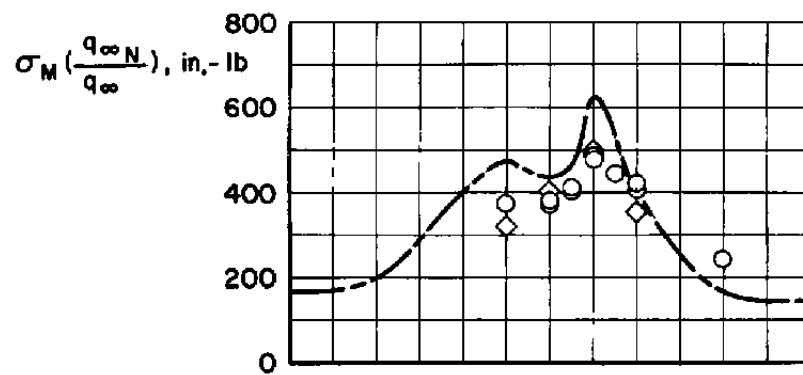


b. In-Phase Response

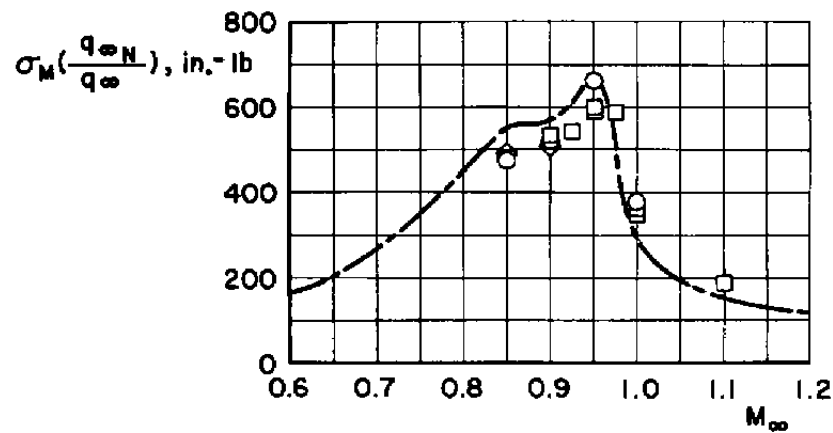
Fig. 28 Variation of the Total Acceleration and In-Phase Response with Frequency, Configuration 46, First Mode



a. Configuration 42

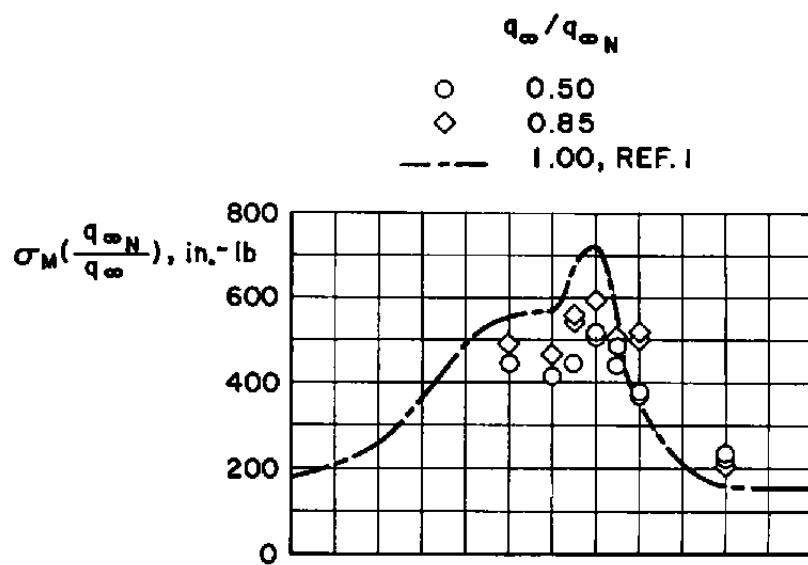


b. Configuration 43

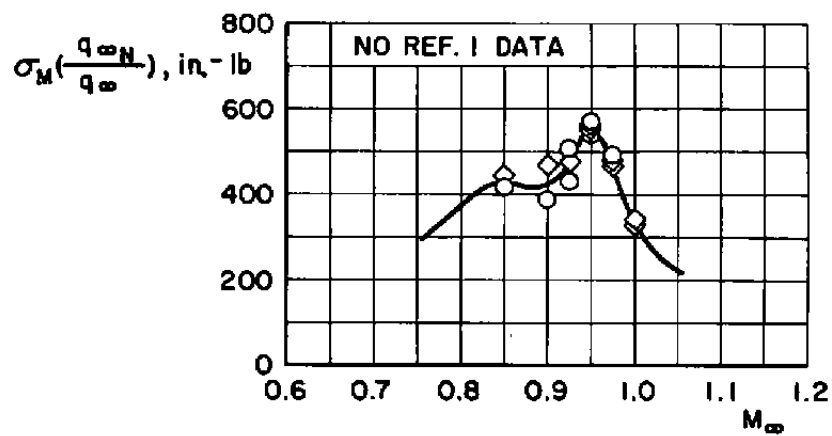


c. Configuration 44

Fig. 29 Variations of the Total Elastic RMS Bending Moment with Mach Number

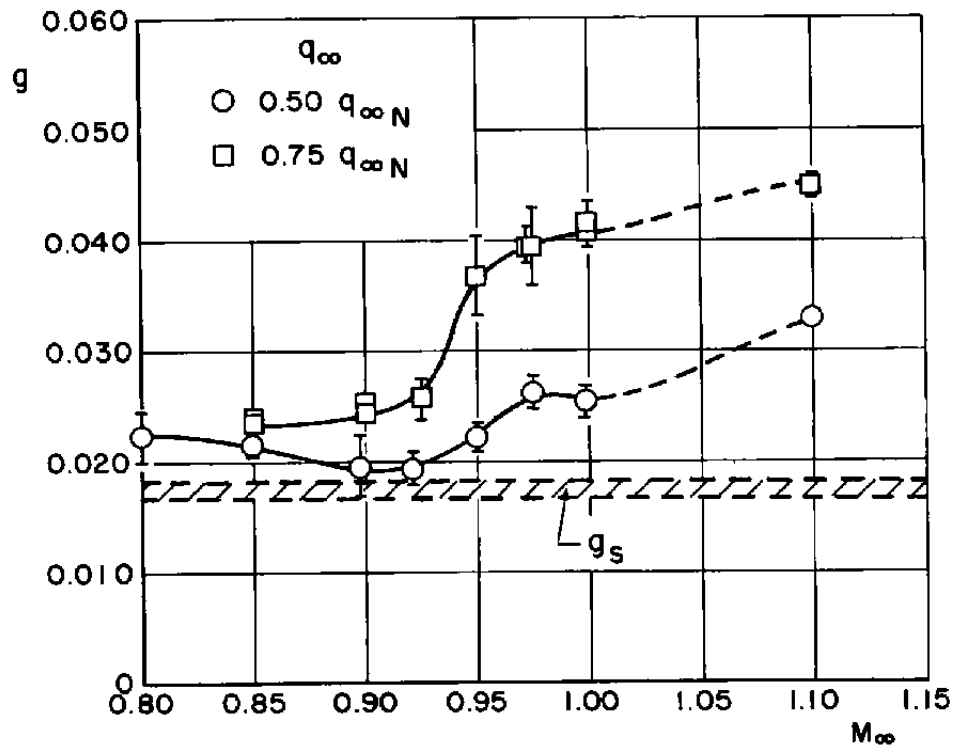


d. Configuration 45

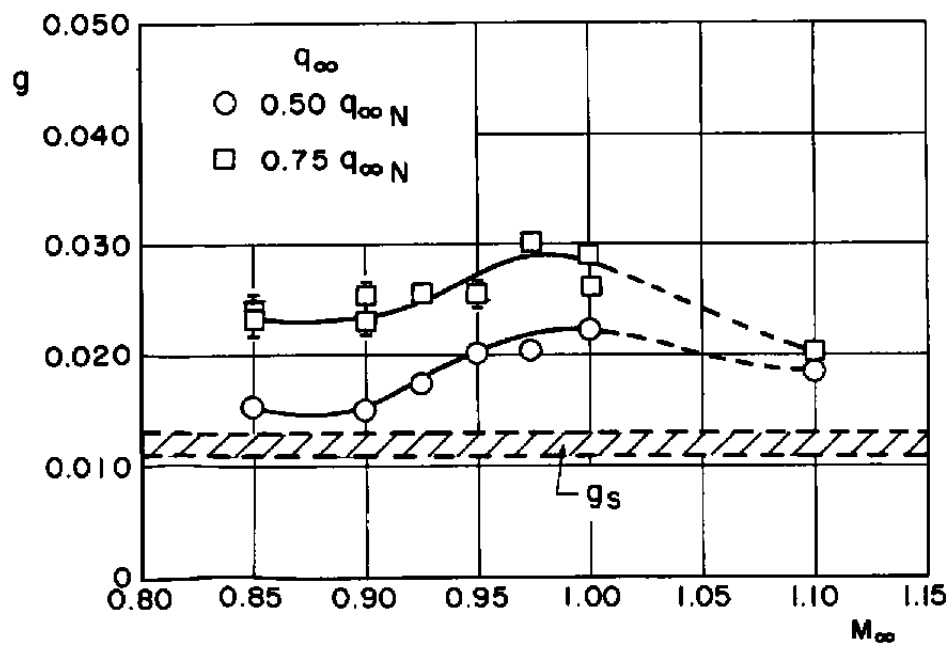


e. Configuration 46

Fig. 29 Concluded

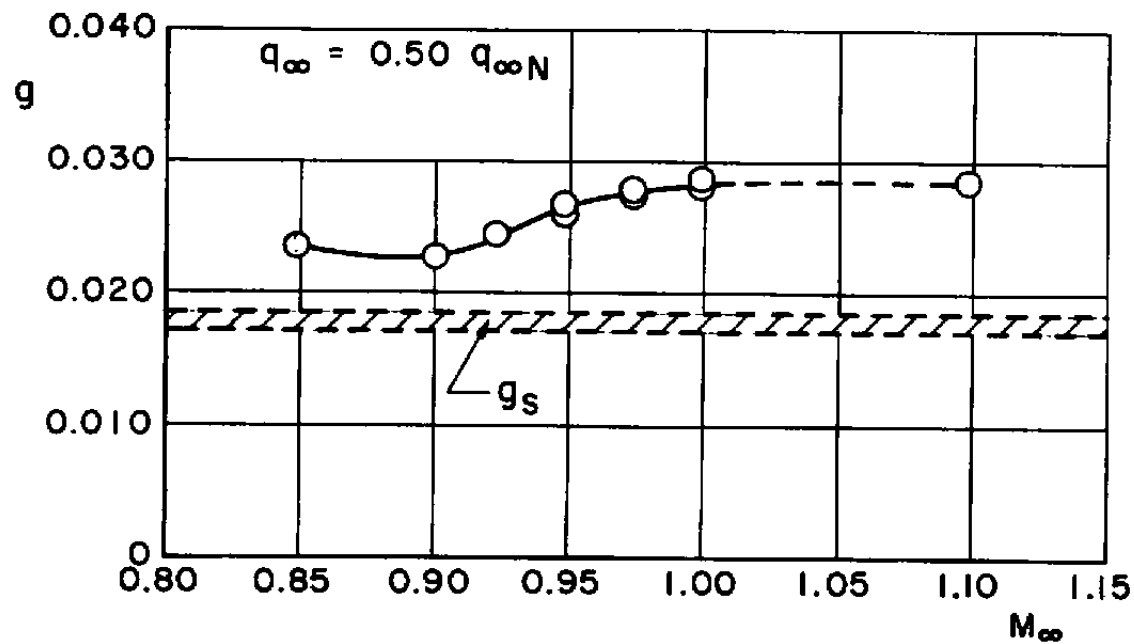


a. First Mode

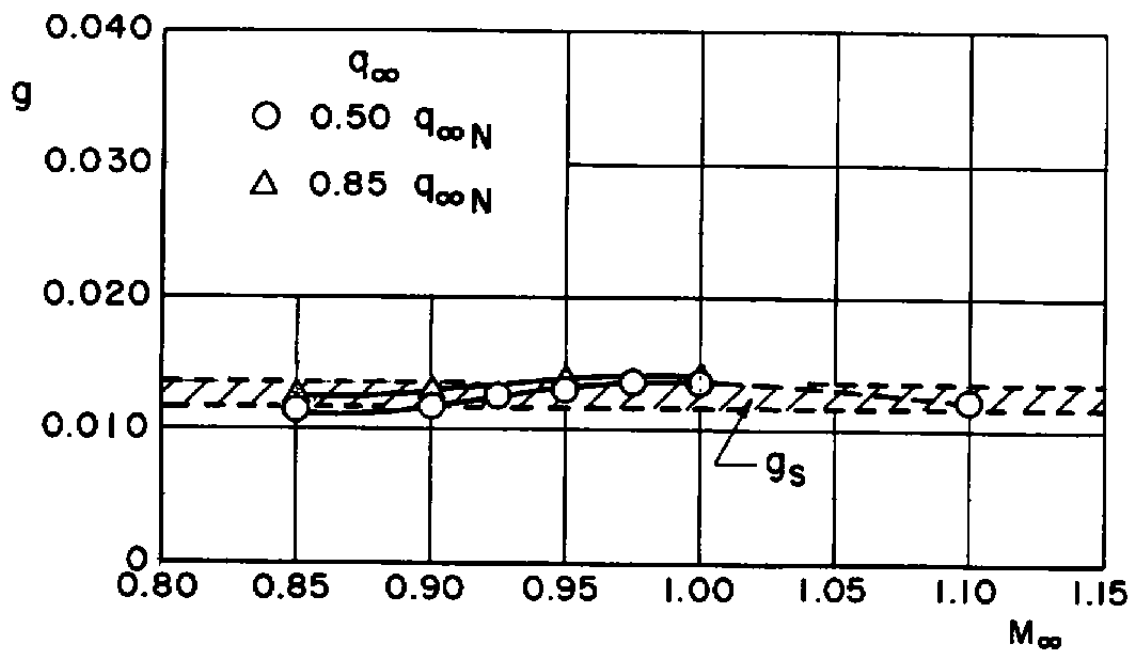


b. Second Mode

Fig. 30 Variations of Total Damping Coefficient with Mach Number, Configuration 42

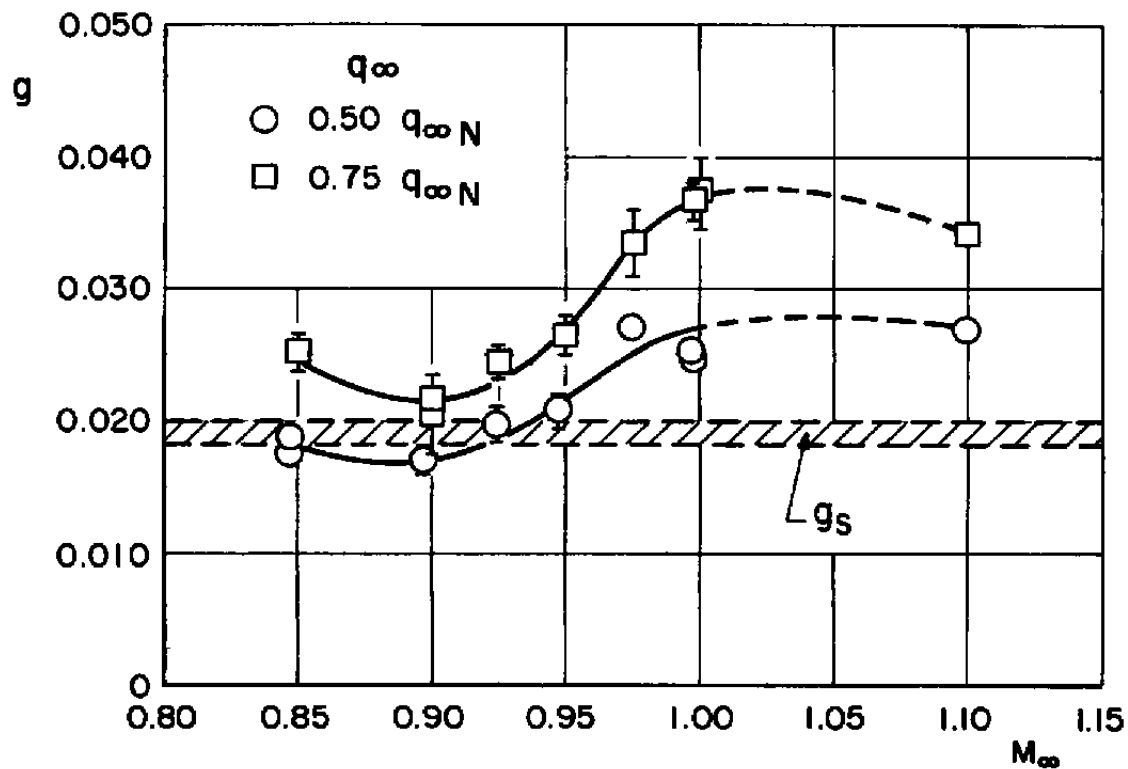


a. First Mode

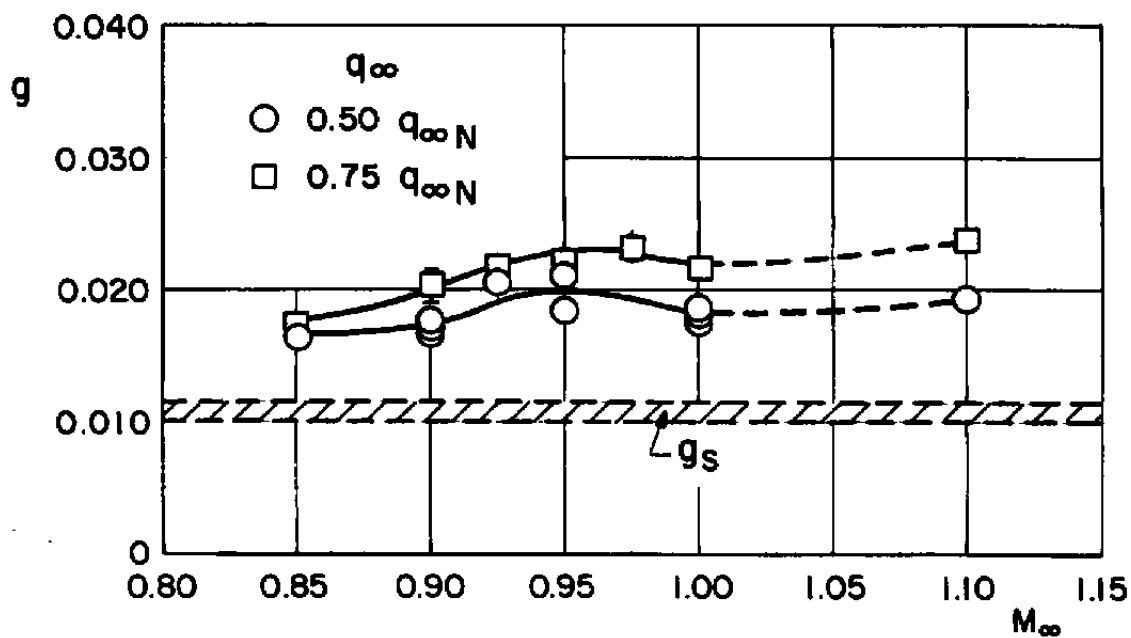


b. Second Mode

Fig. 31 Variations of Total Damping Coefficient with Mach Number, Configuration 43



a. First Mode



b. Second Mode

Fig. 32 Variations of Total Damping Coefficient with Mach Number, Configuration 44

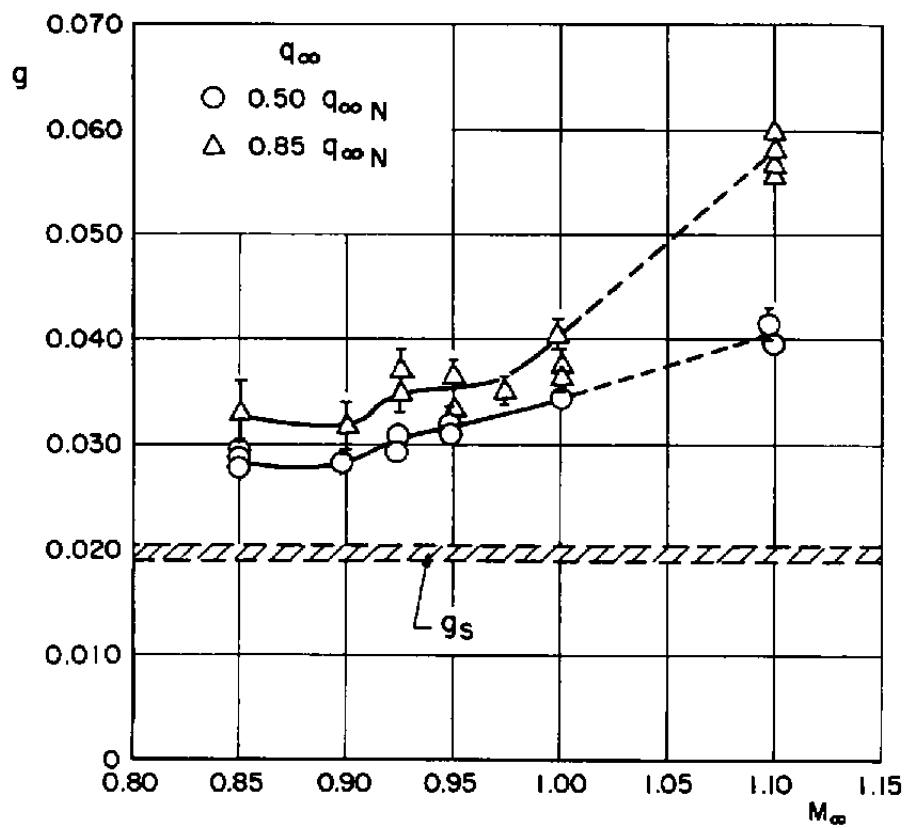


Fig. 33 Variation of Total Damping Coefficient with Mach Number, Configuration 45, First Mode

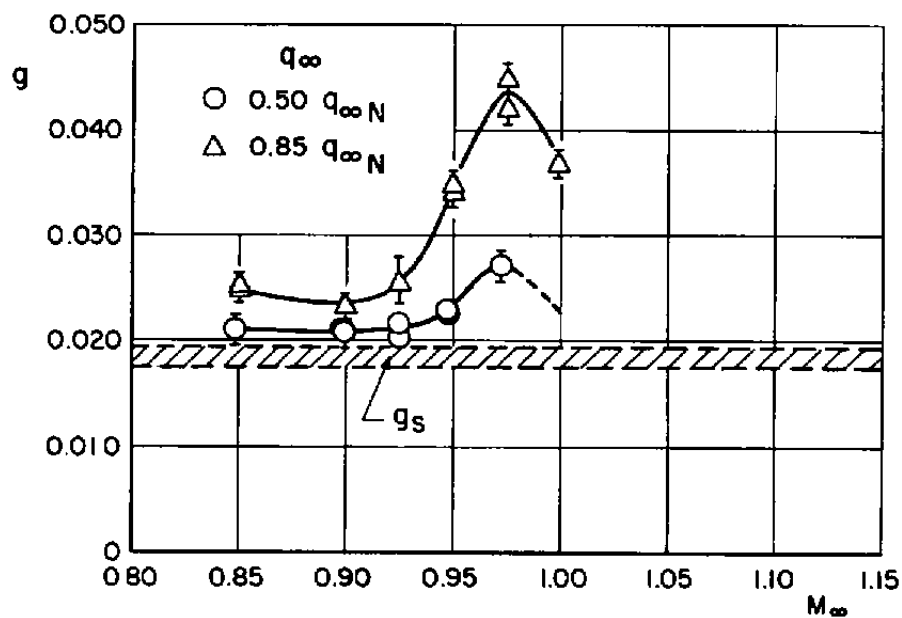


Fig. 34 Variation of Total Damping Coefficient with Mach Number, Configuration 46, First Mode

APPENDIX II

DERIVATION OF MODEL SCALING PARAMETERS

The models were aeroelastically scaled to be dynamically similar to the prototype vehicles. The scale factors used in the model design were dictated by the wind tunnel size and the necessity to match pertinent dimensionless and independent parameters [referred to as $\Pi(\pi)$ terms, Ref. 8]. The descriptive variables and the basic dimensions are:

<u>Symbol</u>	<u>Variable</u>	<u>Dimensions</u>
a_∞	Free-stream speed of sound	LT^{-1}
E	Young's modulus of elasticity	FL^{-2}
f	Frequency	T^{-1}
g	Gravitational acceleration	LT^{-2}
I_a	Area moment of inertia	L^4
I_m	Mass moment of inertia	FT^2L
ℓ	Typical linear dimension	L
M	Total mass	FT^2L^{-1}
m	Mass per unit length	FT^2L^{-2}
T_∞	Free-stream temperature	θ
V_∞	Free-stream velocity	LT^{-1}
α	Angle of attack	Dimensionless
ν_∞	Kinematic viscosity of the free stream	L^2T^{-1}
ρ_a	Mass density of air	FT^2L^{-4}
ρ_s	Mass density of structure	FT^2L^{-4}

where L , T , F , and θ are the basic dimensions of length, time, force, and temperature, respectively.

The following design conditions were considered pertinent:

$$\left(\frac{\ell}{\ell_{ref}}\right)_M = \left(\frac{\ell}{\ell_{ref}}\right)_P \quad (\text{Geometry}) \quad (1)$$

$$\left(\frac{V_\infty}{a_\infty}\right)_M = \left(\frac{V_\infty}{a_\infty}\right)_P \quad (\text{Mach number}) \quad (2)$$

$$\left(\frac{f \ell}{V_{\infty}}\right)_M = \left(\frac{f \ell}{V_{\infty}}\right)_P \quad (\text{Strouhal number}) \quad (3)$$

$$\alpha_M = \alpha_P \quad (\text{Angle of attack}) \quad (4)$$

$$\left(\frac{\rho_a}{\rho_s}\right)_M = \left(\frac{\rho_a}{\rho_s}\right)_P \quad (\text{Mass density ratio}) \quad (5)$$

where M and P denote model and prototype, respectively, and ref denotes a reference parameter. To satisfy tunnel requirements for less than one-percent tunnel blockage, of the model, $(\ell_{\text{ref}})_M = 0.07 (\ell_{\text{ref}})_P$.

From the necessity to match Mach number, Eq. (2), it can be shown that

$$\frac{(V_{\infty})_M}{(V_{\infty})_P} = \left[\frac{(T_{\infty})_M}{(T_{\infty})_P} \right]^{1/2} \quad (6)$$

where T_{∞} is absolute temperature in degrees Rankine. Because of limitations in the test facility, there was a temperature mismatch between the model test conditions and the prototype flight regimes.

This mismatch is considered small, such that $\frac{(V_{\infty})_M}{(V_{\infty})_P} \approx 1.0$.

The bending stiffness and running mass of the model were also the correct scaled values of the prototype vehicle.

$$\left(\frac{EI_a}{EI_{a_{\text{ref}}}}\right)_M = \left(\frac{EI_a}{EI_{a_{\text{ref}}}}\right)_P \quad (7)$$

$$\left(\frac{m}{m_{\text{ref}}}\right)_M = \left(\frac{m}{m_{\text{ref}}}\right)_P \quad (8)$$

The necessity to match pertinent conditions Eqs. (1) through (6) resulted in a mismatch in certain remaining π terms.

For example:

$$\left(\frac{V_{\infty} \ell}{\nu_{\infty}}\right)_M \neq \left(\frac{V_{\infty} \ell}{\nu_{\infty}}\right)_P \quad (\text{Reynolds number}) \quad (9)$$

and

$$\left(\frac{V_{\infty}^2}{g \ell}\right)_M \neq \left(\frac{V_{\infty}^2}{g \ell}\right)_P \quad (\text{Froude number}) \quad (10)$$

The mismatch in Reynolds number implies a lack of similarity in the boundary layers on the model and prototype vehicles. The mismatch in Froude number implies a lack of similarity in the gravity effects or that slosh and "deadweight" are not matched. It was felt that these mismatched conditions were not critical to the nature of the test.

The various parameters of the model are defined as follow:

Scale Factor	$n = 0.07$
Length	$\frac{L_M}{L_P} = n = 0.07$
Stiffness	$\frac{(EI_a)_M}{(EI_a)_P} = (n)^4 = 2.40 \times 10^{-5}$
Mass	$\frac{M_M}{M_P} = (n)^3 = 3.43 \times 10^{-4}$
Running Mass	$\frac{m_M}{m_P} = (n)^2 = 4.90 \times 10^{-3}$
Frequency	$\frac{f_M}{f_P} = \frac{1}{n} = 14.28$
Mass Moment of Inertia	$\frac{(I_m)_M}{(I_m)_P} = (n)^5 = 1.68 \times 10^{-6}$

APPENDIX III DERIVATION OF DAMPING PARAMETERS

Consider the complex form of the equation of motion for a discrete system with single degree-of-freedom, forced oscillation:

$$M\ddot{X} + C\dot{X} + KX = \bar{F}e^{i\omega t} \quad (1)$$

where $\bar{F}e^{i\omega t}$ is the input forcing function acting on the system. A solution of the equation of motion is of the form

$$X = \bar{X}e^{i\omega t} \quad (2)$$

where \bar{X} is the complex amplitude. The first and second derivatives of the solution resolves the velocity and acceleration functions:

$$\dot{X} = i\omega \bar{X}e^{i\omega t} \quad (3)$$

$$\ddot{X} = -\omega^2 \bar{X}e^{i\omega t} \quad (4)$$

Substituting Eqs. (2), (3), and (4) into Eq. (1), and simplifying:

$$\bar{F} = (K - M\omega^2) \bar{X} + i(C\omega) \bar{X} \quad (5)$$

A vector representation of Eq. (5) is presented in the phase diagram, Fig. 14. From the diagram:

$$\sin \beta = \frac{C\omega \bar{X}}{\bar{F}} \quad (6)$$

where

$$\beta = \theta - \eta \quad (7)$$

Combining Eqs. (6) and (7), and expanding:

$$\frac{C\omega \bar{X}}{\bar{F}} = \sin \theta \cos \eta - \cos \theta \sin \eta \quad (8)$$

Also, from the phase diagram:

$$\begin{aligned} \sin \theta &= \frac{\bar{F}_I}{\bar{F}} & \cos \theta &= \frac{\bar{F}_R}{\bar{F}} \\ \cos \eta &= \frac{\bar{X}_R}{\bar{X}} & \sin \eta &= \frac{\bar{X}_I}{\bar{X}} \end{aligned} \quad (9)$$

Combining Eqs. (8) and (9) and solving for the damping:

$$C = \frac{\bar{F}_I \bar{X}_R - \bar{F}_R \bar{X}_I}{\omega (\bar{X}_R^2 + \bar{X}_I^2)} \quad (10)$$

It is evident from the phase diagram, that, at resonance ($\beta = 90$ deg), the damping of a single degree-of-freedom system (Eq. 10) is simply the applied force divided by the velocity of application of the force. Since during the present investigation, the force and acceleration were measured, it is convenient to express Eq. (10) in terms of the real and imaginary components of the force and acceleration. Noting from Eqs. (2) and (4) that the position and acceleration are related by minus the square of the circular frequency, Eq. (10) becomes:

$$C = \omega \left(\frac{\bar{F}_R \bar{A}_I - \bar{F}_I \bar{A}_R}{\bar{A}_R^2 + \bar{A}_I^2} \right) \quad (11)$$

where

$$\bar{A} = -\omega^2 \bar{X}$$

At this point it should be noted that the present test model is a continuous system rather than a discrete system. Therefore, it is necessary to assume that the response of the structure can be represented by the superposition of the responses in its individual modes considering each mode to respond as a single degree-of-freedom system with appropriate excitation. It was noted in Refs. 5 and 6 that this assumption is reasonable for a lightly damped continuous structure, as is the case for the present model, and hence will be made here also. For a continuous system, the damping is given by Eq. (11) if the force and acceleration are replaced by their generalized values. Denoting the generalized values with a subscript g:

$$C = \omega \left(\frac{\bar{F}_{Rg} \bar{A}_{Ig} - \bar{F}_{Ig} \bar{A}_{Rg}}{\bar{A}_{Rg}^2 + \bar{A}_{Ig}^2} \right) \quad (12)$$

During the present investigation, a single force was applied to the model and the acceleration response was measured at a single position on the model. The generalized force and acceleration are related to the measured parameters by:

$$\bar{F}_g = \bar{F} h(\text{MS})_F \quad (13)$$

$$\bar{A}_g = \bar{A} / h(\text{MS})_A \quad (14)$$

where $h(\text{MS})_F$ and $h(\text{MS})_A$ are the normalized modal displacements at the model stations corresponding to the location of the force and acceleration measurements, respectively. Therefore, the damping for a continuous system may be expressed in terms of the measured parameters as:

$$C_n = \omega_n \left(\frac{\bar{F}_{R_n} \bar{A}_{I_n} - \bar{F}_{I_n} \bar{A}_{R_n}}{\bar{A}_{R_n}^2 + \bar{A}_{I_n}^2} \right) h(MS)_{F_n} h(MS)_{A_n} \quad (15)$$

where the subscript n denotes the elastic mode n.

For wind-off conditions, the damping given by Eq. (15) is the equivalent viscous value of the structural damping (C_s). The structural damping coefficient for a given mode is defined for a lightly damped system as:

$$g_s = \frac{2C_s}{C_{cr}} = \frac{2C}{C_{cr}} \bigg|_{\text{air-off}} \quad (16)$$

where

$$C_{cr} = 2\omega M_s$$

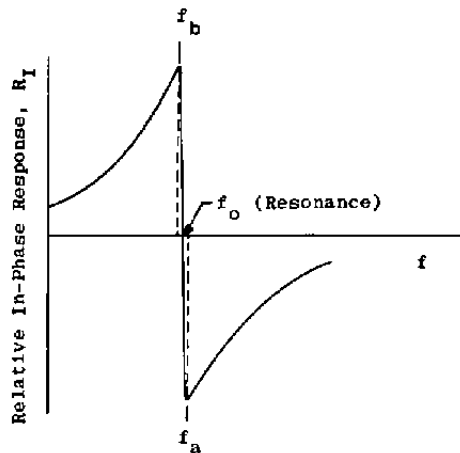
For air-on conditions, the damping given by Eq. 15 is the sum of the structural damping (C_s) and the aerodynamic damping (C_a). The air-on damping coefficient for a given mode is defined as:

$$g = \frac{2(C_s + C_a)}{C_{cr}} = \frac{2C}{C_{cr}} \bigg|_{\text{air-on}} \quad (17)$$

Another method of determining the damping coefficient (g) has been proposed by Stahle (Refs. 5 and 6). Noting that the in-phase response (R_I) peaks at frequencies just below and just above resonance, it can be shown that the damping coefficient may be expressed as:

$$g = \frac{(f_a/f_b)^2 - 1}{(f_a/f_b)^2 + 1} \approx \frac{f_a - f_b}{f_o} \quad (18)$$

Where f_a , f_b , and f_o are defined in the following schematic



It is evident from Eq. (18) that, for a lightly damped system, the peaks occur extremely close to resonance. For example, if $g = 0.018$ and $f_0 = 18$ cps, then $f_a \approx 18.162$ and $f_b \approx 17.838$. Therefore, if the frequency resolution is only ± 0.05 cps which is representative of the uncertainty of the present system, the error in computing g using Eq. (18) could be as large as 30 percent. This problem is further augmented by ill-defined in-phase response curves for air-on conditions. The variations with frequency of the in-phase response were plotted for both air-off and air-on vibrational tests; however, they were used only to evaluate pitch-yaw coupling effects as discussed in Section 4.1.2.

DOCUMENT CONTROL DATA - R & D

(Security classification of title, body of abstract and indexing annotation must be entered when the overall report is classified)

1. ORIGINATING ACTIVITY (Corporate author) Arnold Engineering Development Center ARO, Inc., Operating Contractor Arnold Air Force Station, Tennessee		2a. REPORT SECURITY CLASSIFICATION UNCLASSIFIED	
		2b. GROUP N/A	
3. REPORT TITLE BUFFET RESPONSE AND AERODYNAMIC DAMPING CHARACTERISTICS OF AERO-ELASTICALLY SCALED TITAN III/MOL CONFIGURATIONS AT TRANSONIC SPEEDS			
4. DESCRIPTIVE NOTES (Type of report and inclusive dates) April 27 to May 19, 1967			
5. AUTHOR(S) (First name, middle initial, last name) J. E. Robertson and T. R. Brice, ARO, Inc.			
6. REPORT DATE September 1967		7a. TOTAL NO. OF PAGES 76	7b. NO. OF REFS 8
8a. CONTRACT OR GRANT NO. AF 40(600)-1200		9a. ORIGINATOR'S REPORT NUMBER(S) AEDC-TR-67-178	
b. PROJECT NO. c. Program Element 6440909F/624A		9b. OTHER REPORT NO(S) (Any other numbers that may be assigned this report) N/A	
d.			
10. DISTRIBUTION STATEMENT This document is subject to special export controls and each transmittal to foreign governments or foreign nationals may be made only with prior approval of SAMSO (SMSDM-1) STINFO, AF Unit PO, Los Angeles, Calif.			
11. SUPPLEMENTARY NOTES Available in DDC		12. SPONSORING MILITARY ACTIVITY SAMSO (SMSDM-1) STINFO, AF Unit P.O., Los Angeles, Calif.	
13. ABSTRACT A wind tunnel investigation was conducted to obtain the buffet response and aerodynamic damping of 0.07-scaled aeroelastic models of Titan III/MOL configurations at transonic Mach numbers. Buffet response results were obtained in the form of bending moments at a selected model station. Aerodynamic damping results were obtained by the forced-oscillation technique, whereby the elastic modes of the model were excited by an electromagnetic shaker, and the exciting force and resulting model acceleration were recorded. A phase separation technique was used to resolve the structural damping (air-off conditions) and combined structural and aerodynamic damping (air-on conditions) from the measured force and acceleration. The test was conducted in the Mach number range from 0.80 to 1.10 and at zero angle of attack. All configurations experienced peak buffet response near Mach number 0.95. The buffet response for the Gemini and SV-5 configurations agreed reasonably well with previous test results for the same or similar configurations. The aerodynamic damping was generally positive and varied with Mach number. The largest variations occurred in the Mach number range from 0.925 to 1.00 for the Gemini and SV-5 configurations. Increasing dynamic pressure caused an increase in aerodynamic damping, although the increase in damping was not necessarily proportional to dynamic pressure. Subject to special export controls; transmittal to foreign governments or foreign nationals requires approval of SAMSO (SMSDM-1) Los Angeles, Calif.			

KEY WORDS

LINK A

LINK B

LINK C

ROLE

WT

ROLE

WT

ROLE

WT

Titan III/MOL
buffetting
damping
transonic flow